Scanning Tunneling Microscopy of Metals and Semiconductors

Introduction

Applications of scanning tunneling microscopy (STM) to surfaces of both metals and semiconductors have rapidly expanded during the last fifteen years. Initial STM studies in both cases focused on structural imaging as well as measurement of electronic properties using scanning tunneling spectroscopy (STS). That early work was primarily for low-index surfaces, as reviewed by Hamers [97H1]. Later studies included a much greater range of surfaces and measurement techniques. The following literature overview summarizes the STM/STS studies of crystalline surfaces of metals and semiconductors from 1997 to 2012. The elements and compounds are listed with alphabetical order, and within each material the topics are ordered from lower to higher index surfaces.

Metals

The metal surfaces are rich in physical phenomena and many metallic surfaces are important for adsorbate ordering, nanostructure formation and surface catalysis processes. The focus of STM studies on metal surfaces from 1997 to 2012 varies depending on the type of metal surface or surface index. On some metal surfaces such as Ag(111) and Cu(111), the existence of a two dimensional surface state near the Fermi level influences adatom diffusion, epitaxial growth, equilibrium crystal shapes, reconstructions, surface chemical reactions, and adsorbate ordering processes. STM with its imaging and spectroscopic capabilities is the right choice of instrument to explore the surface state related phenomena on these surfaces, including the surface state lifetime, surface state electron confinement, and the electron standing waves. STM is also used to study the image-potential states on metal surfaces. The 'z' versus V spectroscopic data show the existence of Rydberg-like series of potentials along the surface normal direction on many metal surfaces. The measurements further reveal a strong influence of Stark effect and tip shape on the observed quantized potentials. The dynamic at step edges are also of interest because they can influence the crystal growth. Dislocations at surfaces are also vital in many areas of materials science. For example, screw dislocations can influence the crystal growth, and can modify surface stress. Detailed STM studies for dislocations have been carried out on Ag(111) and Au(111) surfaces. On vicinal surfaces such as Au(110), Ag(110), Pt(110) and Ir(110), the surface roughening and phase transitions are of main interest. The STM measurements are focused on Ising type phase transition and surface roughening transitions at elevated temperatures. On 5d metals such as Au, Pt and Ir surfaces, the top most surface layer often reconstruct due to strain. STM studies on Au(100), Pt(100) and Ir(100) surfaces are mainly devoted to surface reconstruction and related phenomena. On Au(111) surface, the stability of herringbone type reconstruction has been explored by forming vacancy islands. Surfaces having spin density of states such as Ni, Cr, and Fe, the interplay between the spin and local density of state at the surface have been the focus of the studies. The bcc metal surfaces such as Mo, W, and Ta are important for many applications however, preparation of a clean and atomically flat surface for STM studies is difficult. Nevertheless, a number of studies have reported for atomic resolution images on these surfaces as well.

The following literature overview summarizes the STM/STS studies of *bulk* crystal surfaces of *pure* metals. Many STM studies of metal surfaces from 1997 to 2012 are extensions of initial findings that have been reported prior to this period. This overview does not include bulk and surface metallic alloys, thin-films, adsorbates, and nanostructures on metallic surfaces.

Ag, Silver

Ag(100)

Atomically resolved STM images show the expected square lattice arrangement of individual atoms on this surface [06C]. Changes in surface morphology due to ion sputtering process has been investigated using STM topographic images acquired over different sputter conditions and substrate temperatures [01C]. The study shows that periodic pattern of square islands are formed on this surface when sputtering at substrate temperatures between 240 and 440 K.

Ag(110)

STM image of Ag(110) acquired at 300K shows the expected structure of atomic rows running along [110] surface direction [99K, 00K]. On this surface, the role of tip-surface interaction has been studied using an elevated temperature STM [00K, 00S2]. At 360K, the step edges of Ag(110) show several nm long fringes along the scanning direction (Fig. 1) [00K] and this effect is explained as diffusion at step edges induced by the STM tip. At 300K, however, scanning parallel to the closed-pack direction along the step edge does not show any fringes, thus stable step edge can be observed in STM images. Other studies on Ag(110) include the study of surface steps [00B2] and changes in surface morphology due to ion sputtering processes [97R2, 01C].

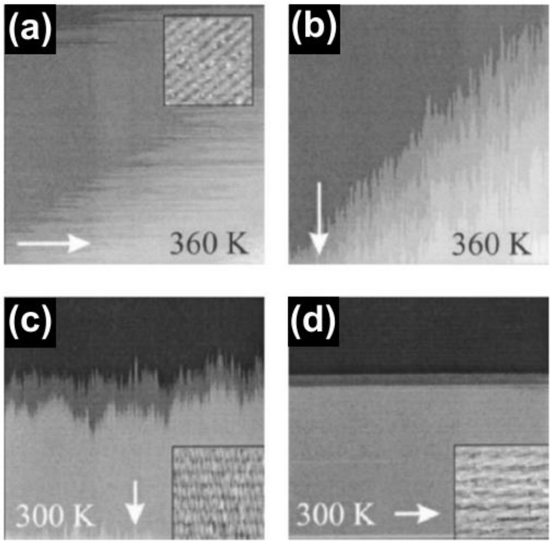

Fig. 1. (a and b) 25×25nm^2 STM images of the same area of Ag(110) at 360±10 K and different fast scanning directions (indicated by arrows) revealing fringy $[1\bar{1}0]$ steps that run parallel to the close-packed rows [-25mV, 1.8nA]. (c and d): 25×20 nm^2 STM images of the same area of Ag(110) at 300 K with the fast scanning direction (indicated by arrows) perpendicular (c) and parallel (d) to the $[1\bar{1}0]$ steps. [−257 mV, −0.5 nA]. The insets show the respective raw data at a higher magnification [00K].

Ag(111)

Ag(111) surface has a Shockley-type surface state around -65 meV, which forms two dimensional nearly free electron gas parallel to the surface and generates many interesting physical phenomena [97L, 98B, 98L3, 8L4, 98L5, 99L, 02M2, 03V]. The surface state of Ag(111) can be directly determined by using dI/dV-V spectroscopy, where the surface state onset appears as a rise in dI/dV signal (Fig. 2) [98L4]. To avoid the influence of defects or step edges, the surface state needs to be determined at large flat terraces [99L]. During the spectroscopic measurements, the changes in the tip positions can alter the barrier transmission probability that can in turn change the positions of dI/dV maxima in the spectroscopic curve. Li et al. [97L] describes a way to correct this by dividing the dI/dV data with the transmission coefficient T, which is defined as:

$$T(E, eV, x) = \exp\left[-z(x)\sqrt{\frac{4m}{\hbar^2}}(\phi_t + \phi_s + eV - 2E)\right].$$

Here, ϕ_t and ϕ_s are the work functions of the tip and the Ag(111) sample, and $z(x) = z_0 + \Delta z(x)$, where z_0 is the tip height. This procedure is applicable only when the measurements are performed at 1 nm or more distance away from a step edge on Ag(111). From the geometric line width of the rise of surface state onset in the dI/dV curve (Fig. 2b), the lifetime of surface state electrons can be determined [98L4, 06B] as well.

These surface state electrons scatter from defects and step edges on Ag(111) and produce interference patterns known as electron standing waves (Fig. 3). The electron standing waves can be directly observed even in normal STM images when acquired at lower biases close to the Fermi energy on Ag(111). At higher biases, however, the tunneling current represents a weighted integral over a range of energies, and the oscillatory signal is smeared out.

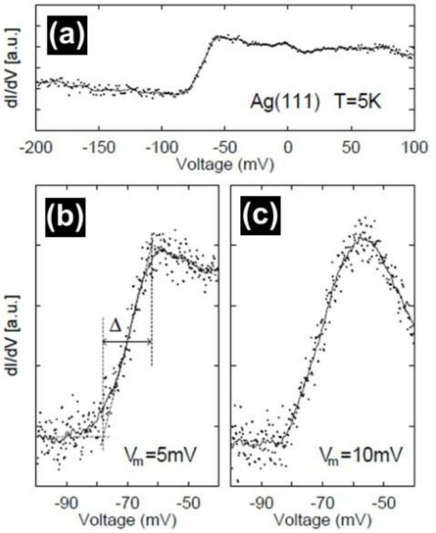

Fig. 2. (a) Surface state of Ag(111) appears as the step-like onset in the dI/dV spectrum. (b) and (c) show the onset region in detail from spectra recorded with different tips, showing the variation in slope above the onset. V_m is the modulation voltage [98L4].

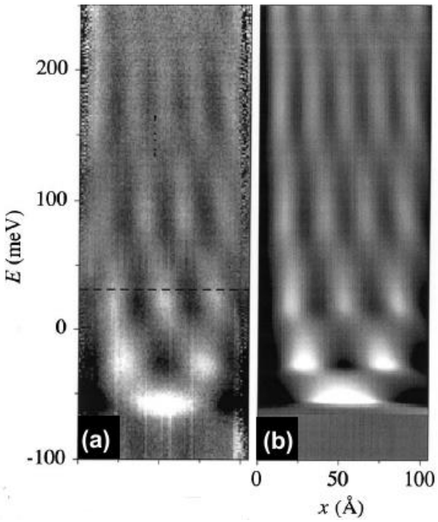

Fig. 3. (a) dI/dV line scan across a Ag(111) narrow terrace measured as a function of bias (E), and (b) corresponding model image [98B].

Morgenstern et al. [02M2] investigated the confinement of surface state electrons in narrow steps of Ag(111). Tunneling spectroscopy data taken over different terrace widthes reveal that the surface state on-set energy is shifted towards the Fermi energy (E_F) when the width is decreased (Fig. 4) due to depopulation of the surface state electrons at narrow terraces. When the terrace width is less than $\lambda_F/2$, where λ_F is the Fermi wavelength of the silver, the electrons can be no longer confined at the terraces because it switches from the terrace to a step modulation of surface electron wave function [02M2].

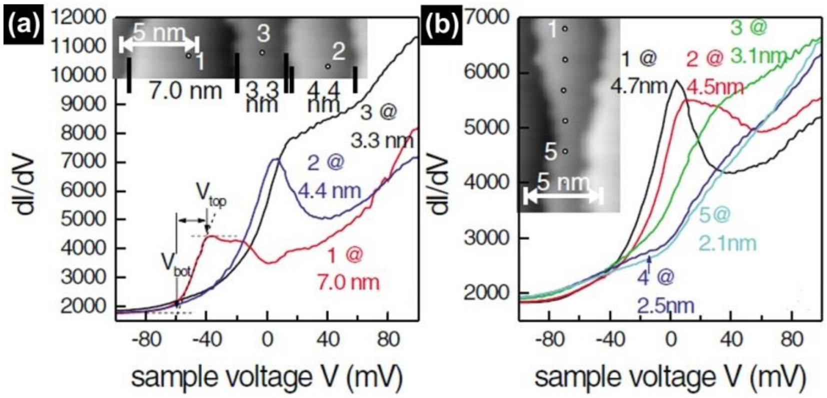

Fig. 4. dI/dV spectra show shifting of the surface state on-set towards the Fermi level when the terrace width is narrower [02M2].

STM is also used to study surface defects such as dislocations. From an atomically resolved STM image of a screw dislocation [02C], the in-plane component of the Burgers vector can be measured (Fig. 5) allowing a direct determination of the Burgers vectors of the individual partial dislocations as $\frac{1}{2}[110] \rightarrow \frac{1}{6}[12\bar{1}] + \frac{1}{6}[211]$ dissociation on $(\bar{1}11)$. In contrast to the normal step edges of Ag(111), which show roughness in STM images indicating diffusions at the steps, the screw dislocation area appears less noisy (Fig. 5). When two mobile dislocations collide, a Lomer-Cottrell lock can be formed, which is a sessile edge dislocation that splits on two different planes. An edge structure that agrees with the expected Lomer-Cottrell lock is also reported [02C]. Moreover, using a fast scanning STM, it is possible to follow the evolution of surface steps [01M2]. For example, the dynamic of a helical step on a Ag(111) surface has been investigated at room temperature [05M]. Generally, a helical step is energetically unfavorable and it is in a non-equilibrium state (Fig. 5). After recording STM images for several hours at room temperature, the change of helical step shape and the coalescence with a vacancy island next to it are observed. The dislocation leads to a long range perturbation of step edge diffusion, and coalescence provides additional supply of atoms accelerating the evolution of the dislocation. Other STM studies include the step edge diffusion processes of Ag(111) islands [00S1, 01M].

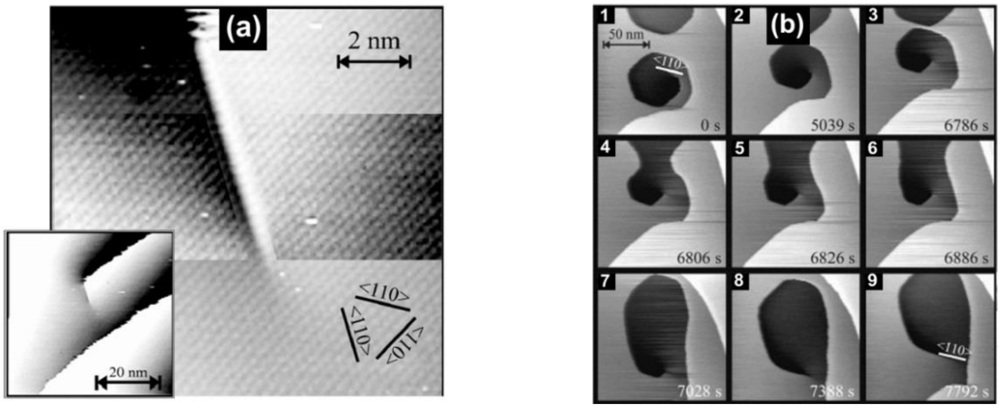

Fig. 5. (Left) Atomic resolution image of the intersection of a bulk dislocation with the Ag(111) surface and its surroundings (inset) [02C]. The Burgers vector is ½ <110>. [-0.22V, 1.4 nA, and T = 330 K]. (Right) Snapshots from an STM movie showing the evolution of a helical step on a Ag(111) surface at room temperature [2.13 V, 0.1 nA, T=320 K] [05M].

Ag(115)

The roughening transition of vicinal Ag(115) surface is investigated by using variable temperature STM by Hoogeman et al. [00H]. The (115) surface consists of (001) terraces with a 2.5 atomic distances separated by (111)-type steps. At elevated temperature, fluctuations of step edges occur resulting in Kosterlitz–Thouless type roughening transition at a temperature of 465±25 K.

Au, Gold

Au(100)

Clean Au(100) forms a reconstruction of its top atomic layer, with a hexagonal geometry on top of the typical square geometry of the bulk lattice plane. The lattice mismatch between the topmost hexagonal layer and the underlying substrate causes strain, resulting in a lateral contraction and buckling of the topmost layer. A high modulation of the topmost layer occurs along [$\bar{1}10$] direction while a smooth modulation with much longer periodicity is found along [110] direction (Fig. 6a) [12B]. González et al. have investigated the collapse of Au(100) surface reconstruction due to the formation of vacancies by ion bombardment [99G]. Upon vacancy formation, the top hexagonal layer becomes instable, and patches of unreconstructed region can be found (Fig. 6b).

Image states of Ag(100) have been determined by means of differential z distance vs. V spectroscopy [07D]. Although Ag(100) exhibits surface reconstruction of the top layer, there is no significant effect is observed in the image-potential states. If there is any spatial variation in image potential due to surface reconstruction, it is not strong enough to influence the image-potential states. The first image-potential state of this surface produces a sharp peak between 5.1 to 5.6 V when measured at different initial tunneling current set-points (Fig. 6c).

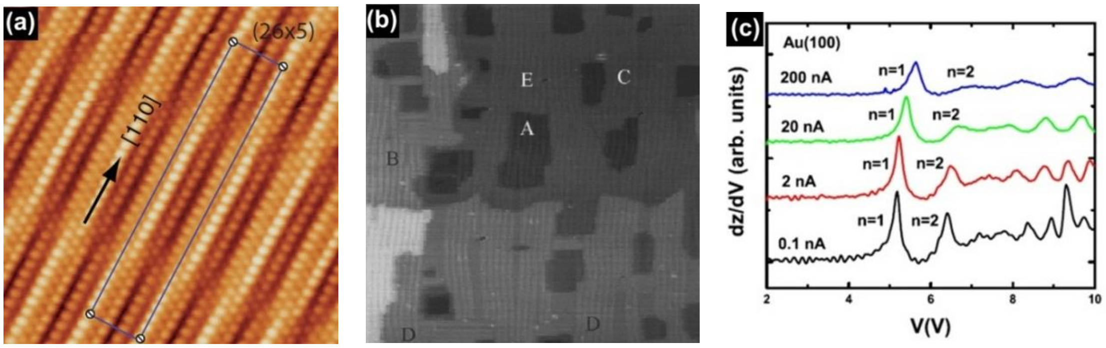

Fig. 6. **(a)** STM image of a reconstructed Au(100) surface [12B]. A (26×5) surface unit cell is shown [10 x 10 nm^2] [12B]. **(b)** STM image of surface defects on Au(100). (A) a vacancy island, and a depression on the right of (B) [99G]. (C) A trough, and unreconstructed patches near (D). (E) A dislocation. **(c)** Image-potential states of Ag(100) showing Rydberg-like series [07D].

Au(110)

The Au(110) surface is known to have (1×2) missing row reconstruction [98K1, 98M, 00K, 01R, 03R], where the alternate atomic rows along [110] directions are missing (Fig. 7) [03R]. A number of STM studies on Au(110) surface have been focused on diffusion of step edges in the missing row reconstruction, and phase transitions [98K1, 00K, 03R]. The Au(110) (1×2) reconstructed surface is known to undergo two phase transitions at elevated temperatures: An Ising transition where the surface deconstructs, and a 3-D roughening transition where the surface no longer exhibits its long-range flatness.

Koch et al. studied Au(110) surface using a high-temperature STM [00K], and it was found that the surface became disordered due to the Ising transition only at the step edges while the (1×2) missing row reconstruction remained on terraces up to the temperatures closed to the 3-D roughening transition at ~700K (Fig. 8). Rost et al [03R] have investigated thermal activated formation of domain boundaries in the missing row reconstruction, which occurs at two special sites: termination sites, and crossing site (Fig. 9). In the termination site, four steps annihilate in one point and in crossing sites, two steps cross each other. From the STM studies of domain boundaries at different elevated temperatures, the Ising and 3-D roughening transition temperatures of Au(110) surface are estimated. The measured Ising transition temperature is in the range between 629 K and 649 K while the 3-D roughening temperature is found in the temperature range between 762 K and 787 K [03R].

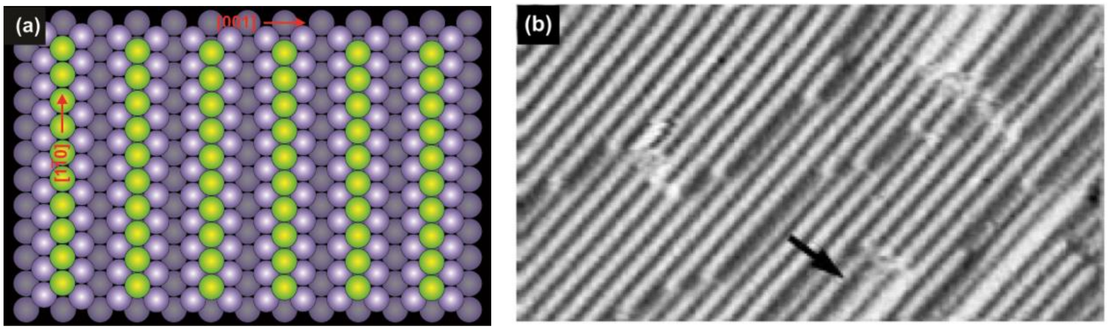

Fig. 7. **(a)** A model of (1×2) missing row reconstruction of Au(110). Green colored atoms are the top rows. **(b)** An STM image of Au(110) reconstruction [98M]. The image shows several terraces with atomic rows along the [110] direction separated by 0.8 nm. At the lower part of the image, two lines are observed with a longer separation of 1.2 nm [indicated with an arrow].

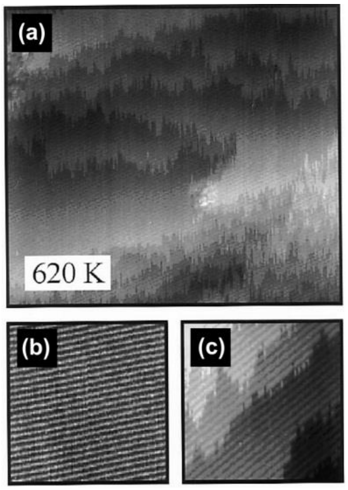

Fig. 8. (a) STM image of Au(110) surface at 620 K [70 x 63 nm^2]. **(b)** (1×2) missing row reconstruction on a terrace of Au(110) at 620K. **(c)** Jagged step profiles at ~550 K [00K].

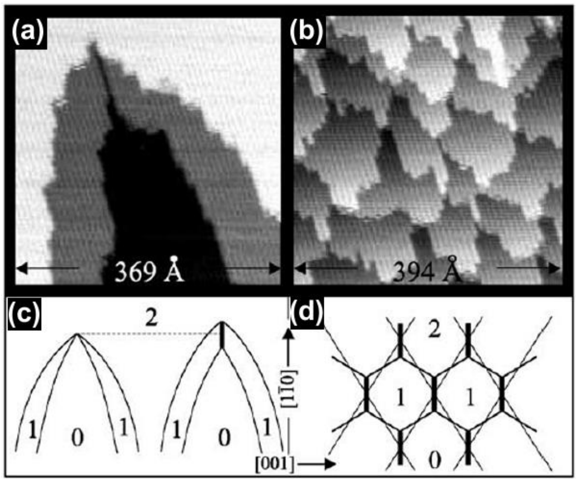

Fig.9. STM images of domain boundaries at the two special sites: **(a)** termination sites (343 K) and **(b)** crossing sites (326 K). **(c)** and **(d)**; Schematics of domain boundary formation at these sites. [03R].

Au(111)

The Au(111) surface is characterized by a hexagonal arrangement of atoms with a herringbone reconstruction (Fig. 10), which is sensitive to the local stress variation as well as the overall surface stress. Engbæk et al. [06E] reported detailed studies of dislocations on this surface. They observed screw dislocations, stacking faults and a Lomer-Cottrel lock. The dislocations can be located from large scale STM images just by following the changes in herringbone reconstruction patterns. An important part in the dislocation studies is the step-height measurements. In general, stacking-fault atoms can be displaced either 1/3 or 2/3 of a full step height on the surface. However, the surface profile under the STM tip is not perfectly perpendicular to the vertical tip direction if there are steps, and a plane fitting is normally required to extract the step-height. For the case of a screw dislocation, the surface plane around the dislocation is inherently tilted and thus it is difficult to perform a plane fitting in order to extract a correct step-height. Engbæk et al. also proposed a simple technique to extract the step height using a LabView program [06E].

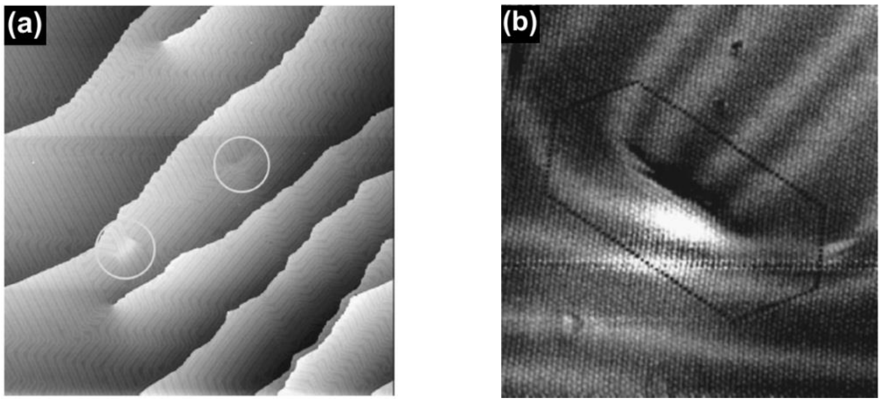

Fig. 10. (a) STM image of Au(111) surface with herringbone reconstruction pattern. The two edge-dislocations are circled. **(b)** An atomic scale STM image of a dislocation on Au(111) [06E].

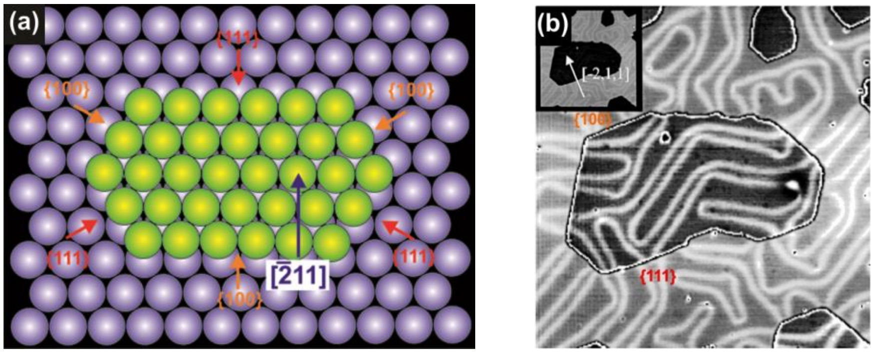

Fig. 11. **(a)** A ball model displaying two types of steps on Au(111). **(b)** STM image of a monolayer deep vacancy island showing {100} and {111} type steps [00R3]. In the {111} type step, the reconstruction lines continue across the step but in the {100} type step, and the reconstruction line either terminate or appear parallel to the step.

In fcc(111) surfaces, the surface steps can have two different types: {111} and {100} types depending on the fcc or hcp stacking of the atoms (Fig. 11a) [00R3]. An ascending step along $[\bar{2}11]$ surface direction is a {100} type step while a descending step along the same direction is a {111} type step. Repain et al. created a monolayer deep vacancy islands on Au(111) surface by sputtering at around 500K to study the reconstruction at step edges. Within an island, both ascending and descending steps along $[\bar{2}11]$ surface direction can be found and thus enabling a direct comparison of the reconstruction behavior at these steps. They observe that the reconstruction lines can cross the {111} type steps (Fig. 11b), however the Au(111) reconstruction lines stop at {100} type steps and occasionally these lines appear parallel to the step. They proposed that the observed surface reconstruction effect on two types of steps can play a role in step dependent faceting behavior of Au(111).

The image-potential states of Au(111) have been measured by Dougherty et al. [07D]. Like in Au(100) surface, the herringbone surface reconstruction of Au(111) does not influence the observed image-potential states. The n=1 image-potential state appears at 5.5 eV. They also recorded the upper band edge of inverted Shockley band gap in the spectra.

Au(788)

The STM image of Au(788) surface shows a uniform array of (111) oriented terraces with similar 3.8 nm width [01M3]. Within the terrace, both fcc and hcp packing produce lighter and darker patches.

Cr, Chromium

Cr(110)

Chromium is a bcc material and an atomically clean Cr(110) surface under ultra-high vacuum conditions is difficult to obtain. Braun et al. [00B1] succeeded to get a well-ordered Cr(110) surface with terraces typically 600 Å in size and segregated contaminant level below 8%, thereby enabling to investigate the surface properties with STM. Atomic resolution STM image of bulk Cr(110) surface show a centered rectangular unit cell (Fig. 12a). The STM images of Cr(110) acquired at low biases near the Fermi level reveal a surface charge density modulation with a corrugation amplitude of 0.15 Å and a periodic wavelength of 42 Å. The wavefronts of these modulations align along the [001] direction on the surface. The modulation amplitude is found to be sensitive on the applied biases, and the wave patterns can be observed over the entire temperature range between 6K and 300K. Moreover, the observed wave patterns are not disturbed or interrupted by steps and defects. Therefore these wave patterns are not related to the Friedel oscillations that produce electron standing waves in fcc metal surfaces such as Ag(111) and Cu(111).

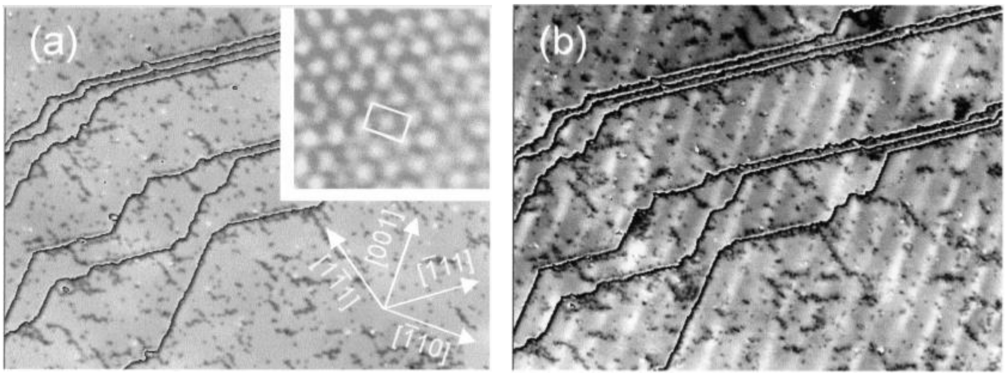

Fig. 12. (a) STM image taken at 6 K [75 x 56 nm^2,1000 MΩ, - 1 V]. The inset shows an atomic resolution [2 x 1.8 nm^2, 0.1 MΩ, 10 mV]. The centered rectangular surface unit cell is marked with a rectangular box. **(b)** The same area as in (a) imaged at reduced sample bias of 210 mV and 10 MΩ tunneling resistance showing surface waves with a wavelength of 42 Å and wave fronts aligned along the [001] direction. The wave pattern is attributed to a surface charge-density modulation arising from the bulk CDW's of Cr with **Q** ∥ [100] and **Q** ∥ [010] [00B1].

Bulk Cr exhibits static spin-density waves (SDW) below the Néel temperature of 311 K due to the wave vector nesting of the electron and hole Fermi surfaces. As a result, the wave vector **Q** is incommensurate with the lattice and it can point along any of the three ⟨100⟩ directions of the bulk Cr lattice. The SDW can be either longitudinal (**S** ∥ **Q** below T_{SF}) or transversal (**S** ⊥ **Q** above T_{SF}) in character, where **S** is the spin polarization and T_{SF} = 123 K is the spin flip transition temperature. The SDW is accompanied by a strain wave and a charge-density wave (CDW) with half the period of the SDW. The observed modulations on Cr(110) surface is identified as surface CDW modulation induced by the two bulk CDW domains with **Q** vector pointing either along the [010] or the [100] out-of-plane direction (Fig. 13). Therefore, the surface domain structure of Cr(110) in its antiferromagnetic SDW ground state has been able to image at the atomic scale in this work.

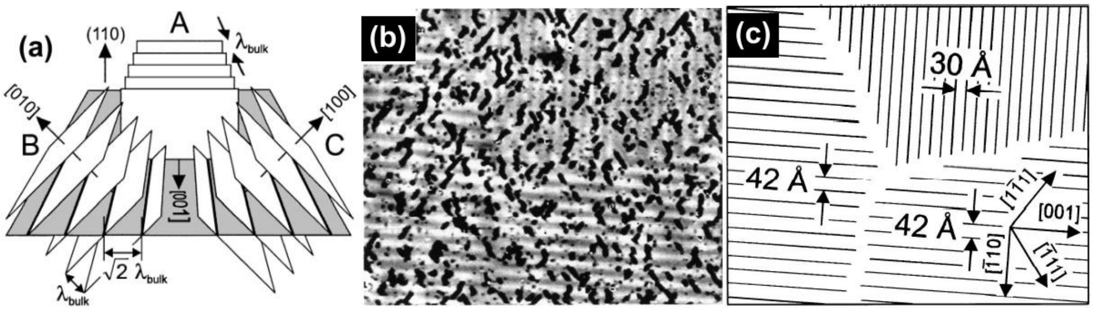

Fig. 13. (a) Schematic wave front arrangement of the three Cr bulk CDW domains (**A**, **B**, and **C**) relative to the (110) surface plane [00B1]. **(b)** 99 x 81 nm^2 surface area [18 MΩ, 20 mV, 135 K] in which the surface CDW with **Q** ∥ [001] (top right) coexists with two dominant CDW domains with **Q** ∥ [100] or **Q** ∥ [010], respectively (left and lower right). **(c)** Scheme of respective wave front positions extracted from (b) [00B1].

Cu, Copper

Cu(100)

The image-potential states of Cu(100) have been measured by Wahl et al. [03W] using distance versus bias tunneling spectroscopy. On this surface, the Rydberg-like series of image-potential states are bound by the tip and crystal potentials along the surface normal direction (z direction). In Fig. 14, the z vs. V curves reveal stair like increases of the tip-height at certain biases starting from 4.7±0.1 V. Since the

STM feedback is turned on during the measurement (constant current mode), an increase in tunneling current causes the tip to retract, thereby the tip-height increases. Thus, the observed stair-case like tip-height curve represents step-wise increases in current originating from some resonance states, which here are the image-potential states. The measured image-potential states are dependent on the initial tunneling current set-points. For instance, two tunneling currents used to measure the z vs V spectroscopy, 0.1 nA and 1.0 nA, produce different voltages for higher-steps (n>1). For the first state (n = 1), both currents provide similar bias values of 4.7 ±0.1 V. The image-potential states are also dependent on the tip-shapes as well. A reason for the energy shifts at the higher states (n>1) is due to the electric field effect of the tip (Startk effect). The quantum interference pattern of the first image-potential state is directly imaged in Fig. 14b [03W], which is generated by the scattering of electrons injected from the STM tip to the first image-potential state.

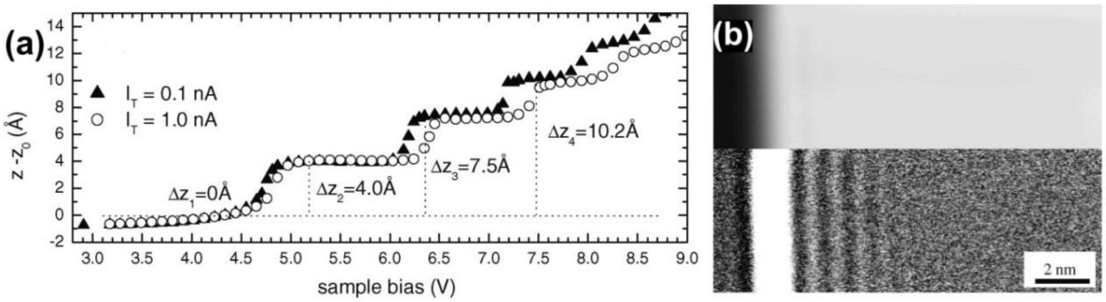

Fig. 14. (a) z versus V curves on a terrace of Cu(100) using two different tunneling currents of 0.1 and 1.0 nA. **(b)** (Top) STM image of a step on Cu(100) acquired at 5.2 V. (Bottom) A dI=dV map of the same place acquired with 5.2V. The image-potential-state electrons reflected at the step edge create a density modulation which appears as a standing wave pattern in the dI/dV map [03W].

Cu(110)

The image-potential states of Cu(110) has been measured by ‘z’ versus V tunneling spectroscopy [07D] (Fig. 15). Like in Cu(100) case, the measurements at different initial tunneling current set-points changes the energies of the higher order states (n>1), however the first image-potential states (n = 1) remain similar. n=1 state on this surface appears rather broad as compared to other surface orientations due to hybridization with the bulk states. Dougherty et al. [07D] suggest that the observed large gap is due to a rapid delocalization of electrons that are transferred from the surface to bulk resonance states.

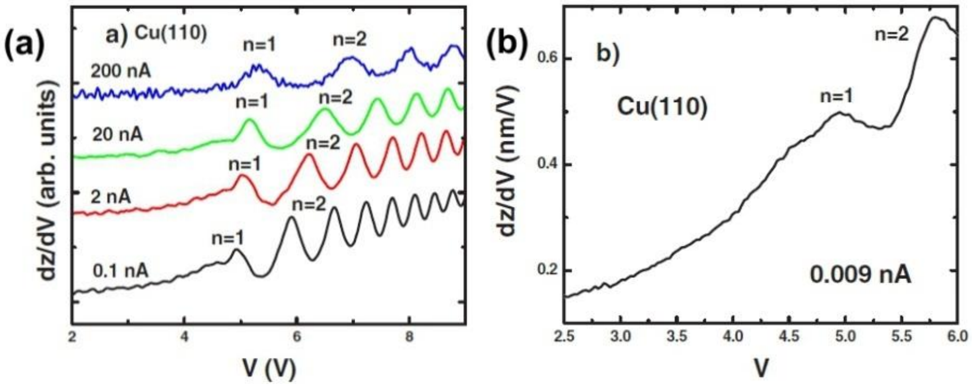

Fig. 15. (a) Differential distance-voltage characteristics measured on a clean Cu(110) surface. **(b)** Differential distance-voltage characteristics measured with tunneling current of 0.009 nA [07D].

Cu(111)

The Cu(111) surface is formed by a hexagonal arrangement of atoms (Fig. 16) with 2.54 Å distance between the nearest neighbor atoms. Like in Ag(111) surface, Cu(111) has a Shockley-type surface state parallel to the surface layer. Two dimensional surface state electrons from this surface state are scattered by defects and step edges generating electron standing waves (Fig. 16) [08A]. The image states of the Cu(111) are measured with the z vs. V spectroscopy on this surface [07D]. Like in Cu(100) and Cu(110), a Rydberg-like series of image-potential states are observed. The first image state (n=1), is observed at ~ 4.4 V. In addition, the observation of a one dimensional edge-state has been reported on this surface [03B1]. STM images acquired at different voltages of step edges of Cu(111) reveal an elongated feature parallel to the step edge on Cu(111) (Fig. 16). Because of the constant current scanned mode, the tip height readjusts with tunneling current by STM feedback. An increase in tip-height, and hence an increase in tunneling current, is observed at both ascending and descending step edges (indicated with arrows in Fig. 16) between 1.5 to 4 V. This observed feature is explained as a localized 1D image state originating from the dipole moment of the step edge, which arises as a consequence of a polarization at the step edge and Smoluchowski smoothing of the electron density [03B1]. Above 4V, the tip height and corresponding current intensity rises due to the image state of Cu(111) surface.

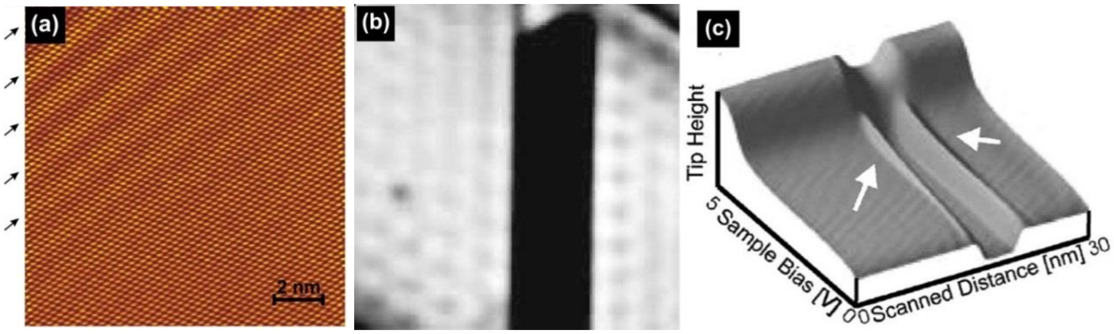

Fig. 16. (a) Atomic resolution STM image of Cu(111) [100 mV, 50 pA, T = 5K] [08A]. Electron standing waves are indicated with arrows. **(b)** A trough on Cu(111) surface with standing electron waves. **(c)** A single line scan measured across the trough in (b) with varying biases from 0 to 5 V is presented as a 3-D plot [03B1].

Cu(115)

STM study on a vicinal Cu(115) surface reveals the expected step structure along the [110] direction separated by (001)-oriented terraces with a step distance of 6.64Å [02R2].

Cu(119)

For the ideal Cu(119) surface, the periodic corrugation of step distance is 11.6Å. Atomic resolution STM image shows the appearance of frizzes due to adatom diffusion along step edges [02R2].

Cu(997)

The ideal Cu(997) surface has monatomic (111) steps along $[\bar{1}10]$ direction separated by (111) terraces with an average terrace width of 18.4Å. However, STM study of this surface [97G2] shows restructuring and faceting of the surface. The authors proposed that the observed restructuring is due to kinetic limitation of the atom motions caused by a large Ehrlich-Schwoebel barrier with self-organization phenomena arising from the strain energy minimization.

Fe, Iron

Fe(100)

Fe(100) surface has majority and minority spin density contributions near the surface Fermi level, and the tip-surface interaction can lead to reversal of atomic corrugation appearance at close sample distances. This effect has been demonstrated by Hofer et al. [01H].

Ir, Iridium

Ir(100)

Ir(100) surface is known to reconstruct and form a (5×1) structure at the top surface layer. STM images of clean Ir(100) surface show atomic rows along [011] direction [00G2, 02S1, 09H]] (Fig. 16). The distance between two consecutive bright row here is as 13.9±0.5 Å, which is five times the next-neighbor distance on the bulk Ir(100)-(1×1) phase. There are two possible models for the arrangement of topmost surface layer with regards to the atomic lattice of underneath layers in Ir(100) (5×1) reconstruction; two-bridge and top-center models (Fig. 17a). From the STM height measurement, the two-bridge model is selected for the atomic arrangement by Gilarowski et al. [00G2], which is further confirmed by Schmidt et al. [02S1]. In Fig. 17b, two atomic rows with the atoms positioning almost at the top sites are resolved while the bridge-site atomic rows between them unresolved. The dark area belongs to the atomic rows in near hollow positions. This (5×1) reconstruction of Ir(100) surface can also be removed and a metastable (1×1) phase can be formed (Fig. 17c) [00G2, 02S1].

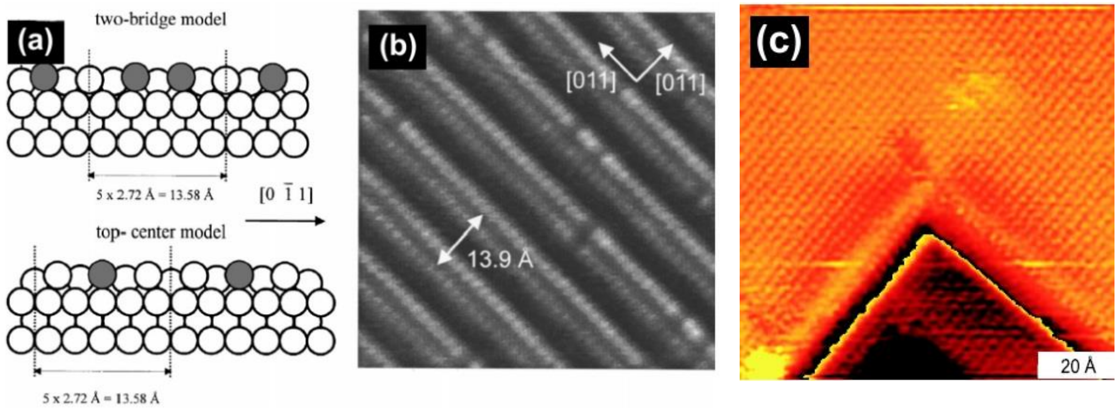

Fig. 17. (a) Possible configurations of the quasi-hexagonal Ir(100)-(5×1) layer (side view). **(b)** An Atomic resolution STM of clean Ir(100)-(5×1) surface [00G2].**(c)** An atomic resolution STM image of Ir(100)-1×1 metastable phase [02S1].

Ir(110)

Unlike the surfaces of Au(110) and Pt(110) that form (1×2) reconstructions, the Ir(110) surface is known to stabilize via {331} facets at room temperature [98K2, 00S3, 02N]. (1×1), (1×3), (1×4) and *c*(2×2) surface reconstruction of Ir(110) also has been reported using various sample preparation conditions [97K], although some of these structures may have been induced by adsorbates. At elevated temperatures between 300K and 1020K, STM investigations reveal a rich variety of surface reconstruction and faceting phenomena (Fig. 18). The ridges produced from {331} facets at room temperature [98K2, 02N] can be flatten by raising the temperature to form (1×3), (1×1) and eventually (1×2) missing row reconstructed terraces at 800 K [00S3, 02N]. At the temperature range between

500K and 600K, droplet-like facets coexist with the (1×3) reconstruction [02N]. At 875 K, STM images show round droplets like structures coexist with (1×2) missing row reconstruction. When the temperature is raised above 900K, the preferential orientation of the surface formed by (1×2) missing row reconstruction disappears, and at 1020 K, kink diffusion occurs.

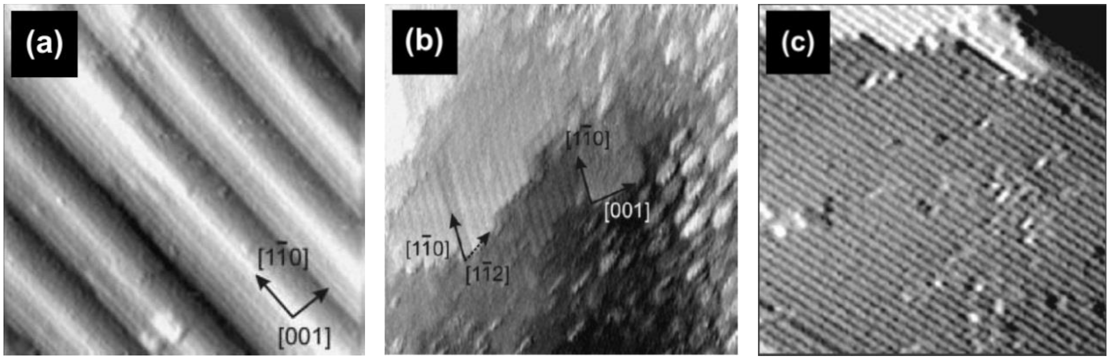

Fig. 18. (a) STM image of Ir(110) at 300 ± 25K showing {331} faceted surface [28 x 28 nm^2]. **(b)** 48 x 48 nm^2 STM image of Ir(110) at 525±30 K showing (1×3) missing row reconstructed areas on the left, a small unreconstructed (1×1) patch in the center, and a droplet covered region on the right [02N]. **(c)** STM image of Ir(110) surface showing (1×2) missing row reconstruction rows below 400K [00S3].

Mo, Molybdenum

Mo(111)

The Mo(111) surface layer is proposed to be relaxed. Although hexagonal-like symmetry is retained, 16.5% and 13.2% contractions of lattice distances as compared to bulk (111) plane in two of the three surface directions occur while the third direction expands for 5.8% lattice distance [06Y]. Atomic resolution STM images of Mo(111) surface reveal a hexagonal symmetry (Fig. 19).

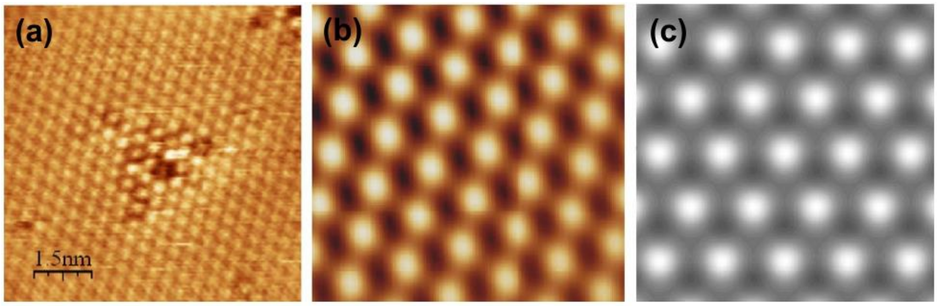

Fig. 19. (a) STM image of Mo(111) surface. **(b)** A zoom in STM image of Mo(111) after Fourier transformation agrees well with calculated image **(c)** [06Y].

Mo(112)

There was a controversy concerning the surface reconstruction of the Mo(112) surface. Initially, Mo(112) surface was reported to be reconstructed [00M1]. However, Yakovkin et al. have shown that the clean Mo(112) surface does not reconstruct [06Y].

Ni, Nickel

Ni(100)

The expected square lattice atomic pattern of Ni(100) surface is resolved in STM images acquired at close tip-surface distances and reduced biases. It is reported that the image contrast could be reversed and the atom could appear as depression or protrusion depending on the tip-state (Fig. 20) [98S1].

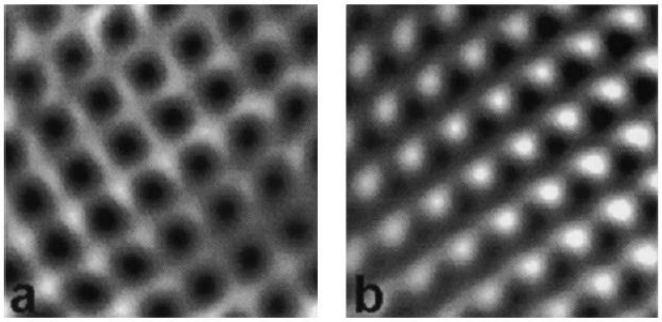

Fig. 20. Atomically resolved STM image of Ni(100) surface acquired at the same tunneling condition shows the atoms as holes in **(a)**, and as protrusions in **(b)** after a tip-change [-20 mV, 1nA] [98S1].

Ni(111)

Ni(111) is a 3d metal ferromagnetic surface, and it is proposed to exhibit a spin-polarized two dimensional electron gas due to a magnetic exchange splitting in the Shockley-type surface state [08B, 09N, 10B]. The electronic structure of Ni(111) investigated near step edges using STS [08B] shows two pronounced maxima close to the Fermi energy. Moreover, Fourier transformations of the surface electron standing waves near the step edges reveal a local dependency of the spin character where the majority spin component predominately exists at an upper step edge close to the step, while on the open terrace, the minority spin component could be found with mixed phases contributed from both spin components. However, the Fourier transformation of electron standing waves scattered by individual defects away from step edges did not show such splitting [09B1]. Thus, it is proposed that the splitting in dI/dV near the Fermi level might be due to the potential difference at the step [09B1]. Electron and hole lifetimes on this surface have been determined by measuring the coherence length of the decaying standing wave pattern at straight step edges of Ni(111) (Fig. 21) [10B]. From the local measurements of surface state lifetimes, it is reported that the hole lifetimes is longer than the electron lifetimes.

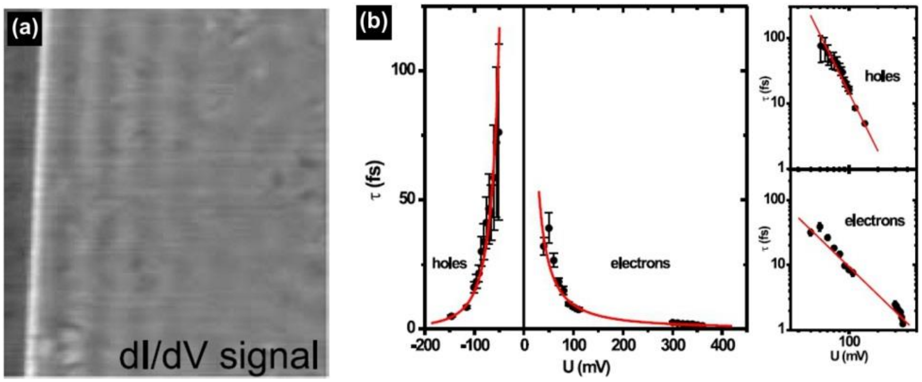

Fig. 21. (Left) A dI/dV map showing standing electron wave front near the step edge. (Right) The plots of electron and hole lifetime as a function of energy at surface state bands of Ni(111) measured from the electron standing wave patterns [10B].

Pd, Palladium

Pd(110)

Dynamics at step edges of a Pd(110) surface has been studied by using atomic scale STM imaging at room temperature [02Y] revealing a mass transport at monatomic step edges perpendicular to the close-packed row directions of Pd(110). The STM image sequence (Fig. 22) shows that the step dynamics are mainly occurring by the diffusion of atoms at the steps perpendicular to the close-packed row directions. Here, the atoms diffuse along the surface troughs to form new islands.

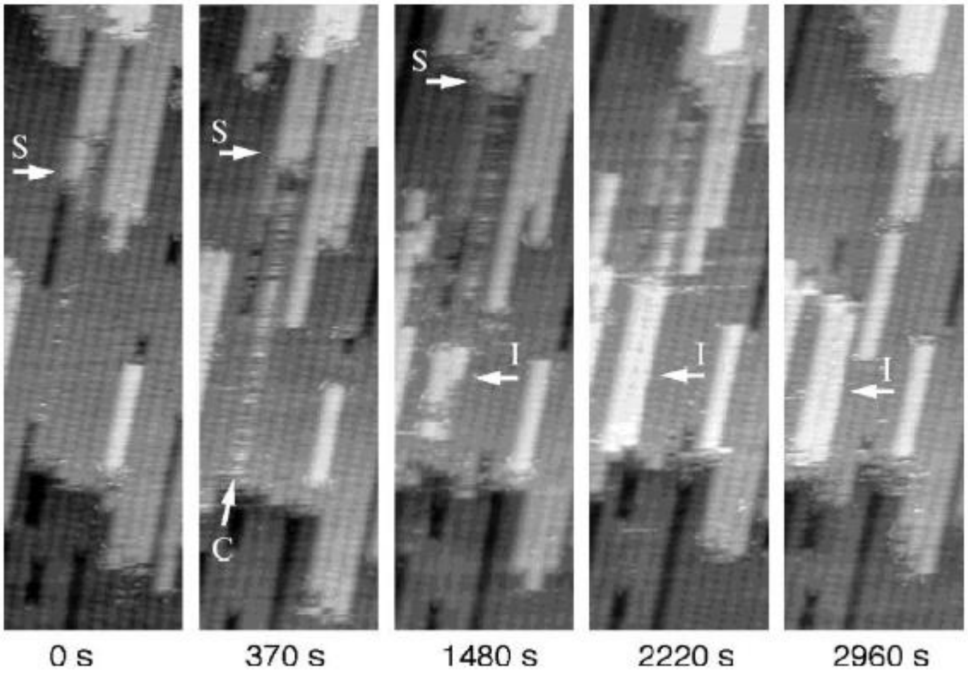

Fig. 22. A sequence of room temperature STM images of Pd(110) surface steps revealing the kinetic at step edges perpendicular to the close-packed surface direction. The marker 'S' indicates detaching atoms from the steps, 'I' indicate addition of the atoms to the new atomic rows, and 'C' indicate diffusing atom [02Y].

The time dependent STM measurements further show that the step fluctuation is limited by the attachment/detachment kinetics at the step edges, and that the step position change follows the power law behavior expressed by $F(t) = [2b^2\Gamma_a / \pi]^{1/2}\, t^{1/2}$ where *F(t)* is the time correlation function, b^2 is the diffusivity of the step, and Γ_a is a friction coefficient representing the detachment rate of an atom from the step. The measured time-dependence of the correlation function is close to a power of 0.5, $F(t) = 0.48\, t^{0.49 \pm 0.02}$.

Pt, Platinum

Pt(100)

Clean Pt(100) surface does not show a square lattice typical to fcc(001) surfaces like Ag(100), and Cu(100). Instead, like in Au(100) and Ir(100) surfaces, the top surface layer forms a pseudohexagonal reconstruction. An STM image of un-rotated Pt(100) reconstructed surface (Fig. 23) reveals a hexagonal arrangement of atoms with a long range modulation along [011] direction [97R1]. The proposed superstructure cell has over 30 atoms in $[01\bar{1}]$ direction (‘**a’** direction in Fig. 28), and 6 atoms in the [011] direction (‘**b’** direction in Fig. 23). The distances of the surface unit cells along ‘***a***’ and ‘***b***’ are about 29 atomic distances and 5 atomic distances of the bulk phase of Pt(100), respectively. This induces a modulation of the corrugation pattern in the unit cell. Ritz et al. [97R1] have found a long range modulation along ‘***b***’ direction having a periodicity of 26 unit cell and half of this distance, 13 unit cells, is marked in Fig. 23. Furthermore they have determined the possibility of reconstruction of the 2nd (sub-surface) layer and have concluded that the sub-surface layer does not reconstruct.

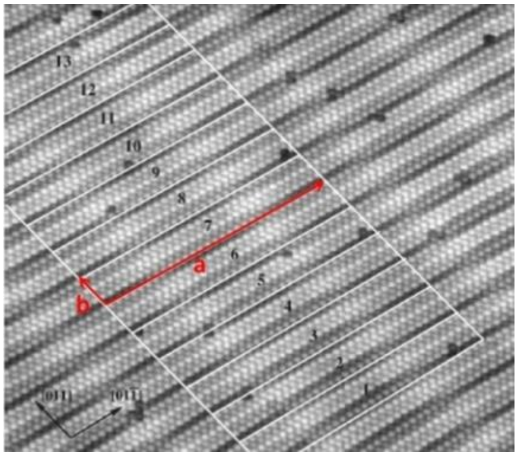

Fig. 23. Large STM scan of the un-rotated hexagonally reconstructed Pt(100) surface. The image size is 20×20 nm^2. ‘***a***’ and ‘***b***’ show a (30×6) unit cell initially assigned. 13 cells of (30×6) surface atoms are marked [97R1].

Pt(110)

Similar to the Au(110), Pt(110) surface reconstructs to form (1×2) missing row structure, and exhibits two phase transitions; Ising and roughing transitions at elevated temperatures. Koch et al [98K1, 00K] investigated Pt(110) surface at elevated temperatures using a high temperature STM. They found that the Ising transition of Pt(110) surface proceeds by simultaneous formation of 2D islands and vacancies on the flat terraces at 725 K (Fig. 24). Fig. 24b shows the existence of an atomic-layer-high islands and vacancies on Pt(110) (1×2) reconstructed surface at 725K indicating that adatom formation is energetically favored on the terraces over the kink sites. Although many defects such as islands and vacancies appear at 725K, (1×2) reconstructed phase is preserved in most of the extended terraces. A 2D roughening transition on this surface occurs only at 850 K (Fig. 24c).

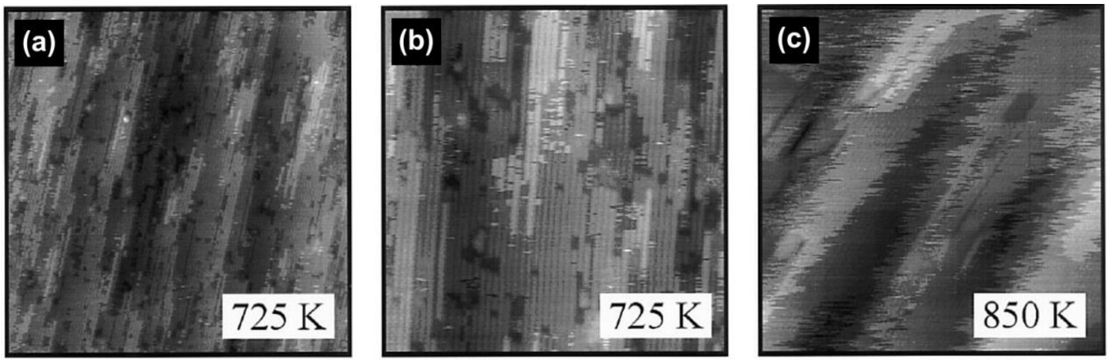

Fig. 24. (a) 80×80 nm^2 and **(b)** 35×35 nm^2 high-temperature STM images of Pt(110) at 725 K displaying many 2D islands and 2D vacancies at (1×2) MR reconstructed terraces. **(c)** 40×40 nm^2 high-temperature STM image of Pt(110) at 850 K showing the beginning of 2D step roughening [scan parameters: 526 mV, 1 nA] [98K1].

Ta, Tantalum

Ta(112)

STM study of clean Ta(112) surface at room temperature indicates instability of the surface [06K], and shows linear atomic chains along the surface troughs, which are probably diffused from the step edges. Kuchowicz et al [06K] proposed a relaxation of the topmost surface layer by creation of (110) micro-facets along the $[\bar{1}11]$ direction and probable rearrangement from (110) bcc to (111) fcc facets.

V, Vanadium

V(100)

Preparation of an atomically clean surface of V(100) is extremely difficult [01B1, 02B]. The (5×1) reconstructed V(100) surface was initially considered as a clean reconstructed surface however, it is induced by surface contaminants such as oxygen [01D, 03K2]. dI/dV tunneling spectroscopy data on a clean V(100) surface area reveals a sharp surface state peak at -0.03eV, just below the Fermi level [01B1, 02B].

W, Tungsten

W(110)

Achieving clean and atomically flat W surfaces is difficult. Cleaning procedures of W surfaces typically involve annealing in an oxygen atmosphere. Oxygen reacts with adsorbed carbon from the surface to form CO and CO_2, which are then desorbed from the surface. Upon removing C, the W surface oxidizes. Removal of oxygen is realized by a rapid high-temperature annealing (flashing) above 2300 K [07B2]. dI/dV map of relatively clean W(110) surface reveal electron standing wave patterns scattered by defects, adsorbates, and step edges (Fig. 25). The observed standing wave is produced by the downward dispersing electron band with an upper band edge of $E_0 = 314 \pm 12$ meV and an effective mass of $m_{eff} = -1.15 \pm 0.05m_e$. This band generates a p_z–d_{xz}-like surface resonance [07B2].

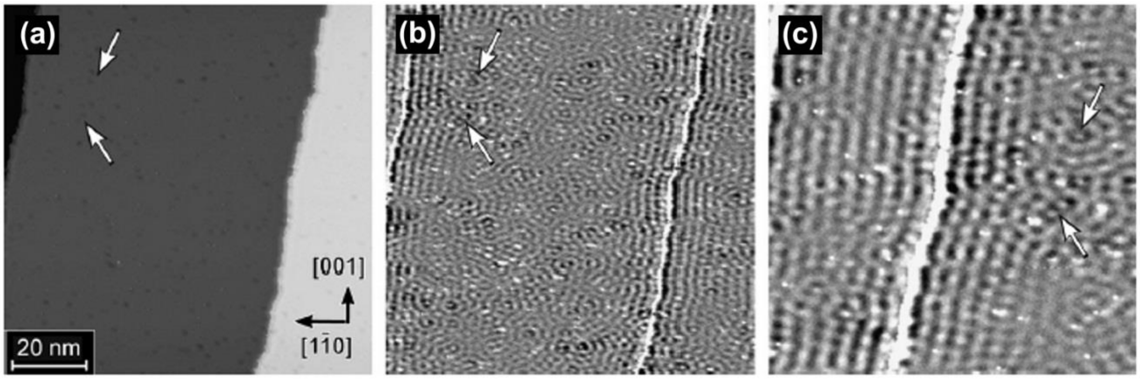

Fig. 25. (a) Constant-current topographic image and **(b)** the simultaneously measured dI/dV map of a clean W(110) surface (I = 1 nA, U = +100 mV). The dI/dV map of the region around the two arrows is shown at higher magnification in **(c)**. The arrows mark some surface impurities [07B2].

W(112)

A clean W(112) surface has been prepared by repeated cycles of annealing in oxygen followed by flashing to ~2500 K, and then the surface was imaged with STM [03Z2]. Atomic structure of the surface is seen in the STM images.

Semiconductors

One means of classifying STM work on semiconductors can be achieved based on the method of preparation of the surface. Surfaces prepared by cleaving in ultra-high vacuum are generally *not* reconstructed, such as the (1×1) surface of GaAs(110). Prominent examples of surfaces that *do* reconstruct upon cleavage are the (2×1) surfaces of Si(111) and Ge(111). Aside from preparation by cleaving, some elemental semiconductor surfaces can be prepared by simple heating (annealing). For *compound* semiconductors, however, it is generally necessary to deposit the constituent species onto a starting surface, often accomplished by molecular beam epitaxy (MBE). In this way, the full range of stable surface structures can be achieved, e.g. for GaAs(001) surfaces ranging from Ga-rich to As-rich. Finally, for the case of the high-index surfaces discussed below, these are often found as small facets that have formed on a growth surfaces of some other (lower index) orientation. This overview focuses on clean (bare) surfaces, although it also includes brief mention of dislocations, electrochemistry, accumulation layers, quantum dots, and dynamical studies.

When referring to polar surface orientations in compounds, the location of the first element of the chemical formula (the cation) is taken to be at the origin of the unit cell. For example, the [111] direction in zincblende GaAs refers to the direction from Ga to As, and similarly the [0001] direction in wurtzite GaN refers to the direction from Ga to N. Thus, a bilayer of atoms on the GaAs(111) surface in bulk-terminated form would have Ga terminating the bilayer. That surface is also referred to as (111)A in the literature. The opposite $(\bar{1}\bar{1}\bar{1})$ surface having As atoms terminating the bilayer is sometimes called (111)B. Similarly, a bilayer of atoms on the wurtzite GaN(0001) surface in bulk-terminated form would have Ga terminating the bilayer, and a bilayer of atoms on the $(000\bar{1})$ surface in bulk-terminated form would have N atoms terminating the bilayer. All surfaces written with three axes refer to cubic (diamond or zinc-blende) crystal structures, whereas all surfaces with four axes refer to hexagonal (wurtzite or more complicated stacking for the case of SiC) crystal structures. For high-index surfaces such as (2 5 11), we write those as (2,5,11), for clarity.

AlAs, Aluminum Arsenide

AlAs(100)

AlAs(100) surfaces have been imaged, as part of a study of the AlAs-on-GaAs (normal) compared to GaAs-on-AlAs (inverted) interfaces [96B]. Upon deposition of the AlAs the RHEED pattern changes gradually from the usual (2×4) As-terminated surface to a weak (2×3) pattern, and an increase in surface disorder is observed. The STM images also reveal areas of exposed Al and/or Ga planes.

AlN, Aluminum Nitride

AlN(0001)

AlN(0001) surfaces prepared under Al-rich conditions reveal $(2\sqrt{3}\times2\sqrt{3})R30°$ and $(5\sqrt{3}\times5\sqrt{3})R30°$ reconstructions [03L1], the latter shown in Fig. 26. These structures are believed to consist of a laterally contracted Al adlayer structure, similar to what occurs on Ga-rich GaN(0001) [00N,08R]. Under N-rich conditions, $(\sqrt{3}\times\sqrt{3})R30^\circ$ and (2×2) reconstructions are observed.

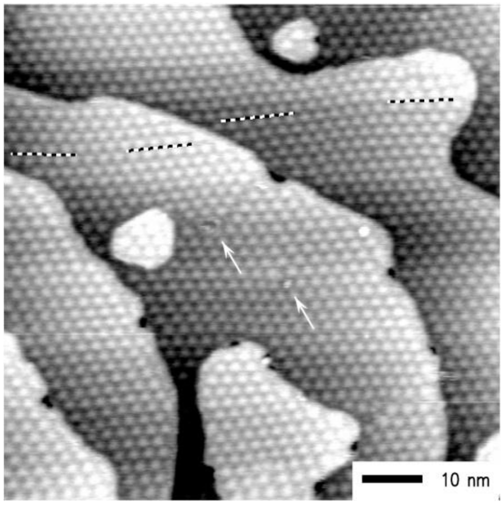

Fig. 26. STM image of Al-rich AlN(0001) surface, displaying the $(5\sqrt{3}\times5\sqrt{3})R30^\circ$ reconstruction. Sample voltage is 1.5 V and gray scale range is 3.5 Å. Some distortions in the hexagonal stacking sequence are marked by dashed lines, and the arrows mark surface dislocations [03L1].

AlSb, Aluminum Antimonide

AlSb(100)

Early studies of AlSb(100) surfaces revealed $c(4\times4)$ and (1×3) surfaces [97T]. The latter are similar to the anion-dimer-based surfaces that also occur on GaAs(100) [97H1,97X,99J], whereas the latter consists of Sb dimers on top of an Sb-dimer-terminated surface. This surface, as well as the corresponding GaSb(100) surfaces, are expected to be metallic, somewhat unusual for a semiconductor surface reconstruction. The influence of the metallic Sb was seen in an STM-based electrochemical study [06M].The same surface reconstructions were observed in a later work [98N2], and interfaces of InAs-on-AlSb and AlSb-on-InAs were also studied.

C, Diamond

C(100)

As an insulator, diamond is difficult to image with the STM. However, the hydrogenated (100) surface can be readily imaged since it has a conductive surface layer, and a (2×1) reconstruction consisting of H-terminated C dimers is observed [03B2]. Even in the absence of the hydrogen termination, STM imaging is possible at elevated voltages, and atomic resolution is obtained for voltages near that of the lowest standing-wave resonance in the vacuum [01B2].

CdSe, Cadmium Selenide, and CdS, Cadmium Sulfide

CdSe($11\bar{2}0$), CdSe($10\bar{1}0$), and CdS($10\bar{1}0$)

Cleaved surfaces of wurtzite CdSe($11\bar{2}0$), CdSe($10\bar{1}0$), and CdS($10\bar{1}0$) were studied by Siemens et al. [97S1]. Non-reconstructed (1×1) structures were observed in all cases. Dopants and defects were also studied.

GaAs, Gallium Arsenide

GaAs(100)

The (100) surface of GaAs terminated predominantly by As dimers serves as a prototype structure for many other compound semiconductors. Early work on these surfaces, prepared by MBE, was reviewed by Hamers [97H1], Xue et al. [97X], and Joyce et al. [99J]. Dynamical studies have been performed on these surfaces [03T]. Surfaces prepared by metalorganic vapor-phase epitaxy (MOVPE) display similar reconstructions as the MBE-grown surfaces [98L2]. Reconstructions of $In_xGa_{1-x}As$ alloy surfaces with x=0.27 and 0.81 have also been studied. [04M].

GaAs(111) and GaAs($\bar{1}\bar{1}\bar{1}$)

Both the (111) and the ($\bar{1}\bar{1}\bar{1}$) surfaces of GaAs exhibit 2×2 reconstructions, with the latter also exhibiting a $(\sqrt{19}\times\sqrt{19})R23.4°$ structure, as observed in early work reviewed by Hamers [97H1] as well as in more recent work [97A,01O,01F]. For InAs on GaAs(111) , an array of misfit dislocations form at the interface due to the strain between the InAs and the GaAs, as shown in Fig. 27c [97Y1].

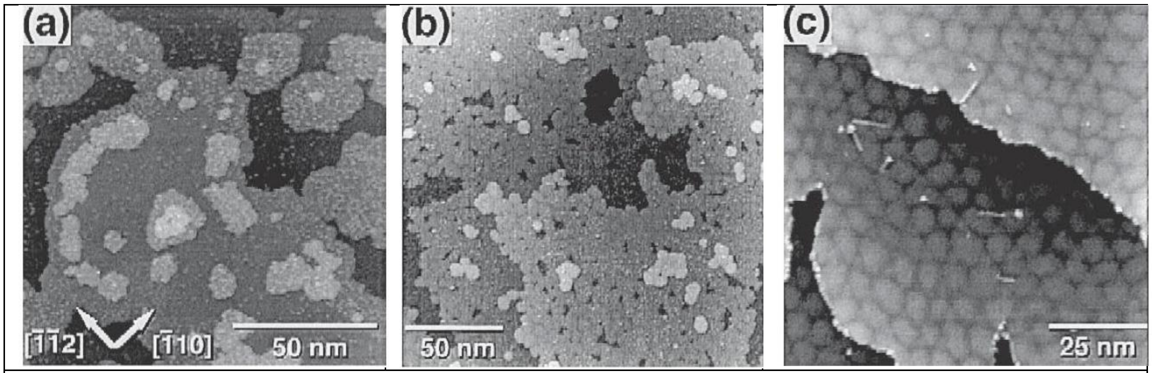

Fig. 27. STM surface topographs of GaAs(111) after the growth of (a) 0.5 ML, (b) 2 ML, and (c) 5 ML of InAs obtained with sample voltages of –1.5 to –3.5 V, and tunneling currents of 0.08–0.2 nA [97Y1].

GaAs(112), ($\bar{1}\bar{1}\bar{2}$), (113), ($\bar{1}\bar{1}\bar{3}$), (114), {137}, (2,5,11), ($\bar{2}$,$\bar{5}$,$\bar{1}\bar{1}$)

STM studies have been performed on various high-index surfaces of GaAs. The (112) and ($\bar{1}\bar{1}\bar{2}$) surfaces are found to be relatively unstable, decomposing into facets of {110}, (111), and {124} orientation [99G,00J]. The (113) and ($\bar{1}\bar{1}\bar{3}$) surfaces exhibit (8×1) reconstructions, and both surfaces have been employed as substrates for quantum dot or quantum wire formation [95W,00M2, 02M1,02S2]. The (114) surface reconstructs as *c*(2×2), with structure related to that of the (001) surface [00J]. {137} surfaces have been observed, as bounding facets on quantum dots [01M1]. Both (2,5,11) and ($\bar{2}$,$\bar{5}$,$\bar{1}\bar{1}$) surfaces have been formed, again as substrates for quantum dot or quantum wires [05T] .

GaN, Gallium Nitride

GaN(0001) and ($000\bar{1}$)

The (0001) and ($000\bar{1}$) surfaces of GaN have been studied over the full range of surface stoichiometry from N-rich to Ga-rich. It is found that, under nearly all conditions, the surface are terminated by Ga atoms, the reason being that for surfaces terminated by N it is energetically favorable for the N atoms to combine as N_2 and desorb from the surface [97S2]. For (0001), the most Ga-rich surface has a full layer of metallic layer on the surface, in the form of a laterally contracted adlyer [98S2,00N,08R]. At room temperature the Ga atoms in this adlayer are in motion, and electron diffraction indicates an incommensurate structure for the adlayer. Under less Ga-rich conditions a sequence of surface reconstructions is observed: (2×2), (5×5), and (6×4) [99S]. These reconstructions are found to be very sensitive to surface contamination [00X,00R1]. A number of interesting topographic features relating to island formation and/or dislocations have been observed on these surfaces [99H,99X,08L].

GaN($10\bar{1}0$)

The ($10\bar{1}0$) surface of GaN has been prepared both by MBE growth and by cleavage. In the former case a somewhat complex reconstruction is found with approximate (4×5) symmetry [03L2]. In the latter case, the surface is not reconstructed [08I,09B2,09E]. Topographic and spectroscopic features relating to contamination, as well as to dislocations and doping, are observed on these cleaved surfaces.

GaP, Gallium Phosphide

GaP(100)

The (100) surface of GaP prepared by MBE has been studied with STM much less thoroughly than for other III-V surfaces. For the Ga-rich surface the data appears to support a mixed dimer model, whereas for the P-rich surface a (2×1)/(2×2) reconstruction with characteristic zig-zag features is seen [01T].

GaSb, Gallium Antimonide

GaSb(100)

The GaSb(100) surface prepared by MBE has been studied as a function of increasing temperature, revealing (2×5), (1×5), *c*(2×6), and (1×3) reconstructions [97T]. The latter three structures are believed to consist of Sb dimers sitting on top of an Sb-terminated surface, whereas the (2×5) structure is found to be composed of Sb dimers on top of *two* layers of Sb. This structure is unique among III-V surfaces, and it is argued to form because of its excellent lattice match with trigonally bonded elemental Sb.

Ge, Germanium

Ge(100)

New STM results for Ge(100) are summarized in [03Z1]; the basic structure is the same as reported by Hamers [97H1], but new phenomena relating to flipping of the dimers and to step edges are presented.

Ge(110)

The (110) surfaces of Ge and Si represent what is arguably the most complex structure of the low-index surfaces of elemental semiconductors. Reconstruction of both surfaces are approximately (16×2), but for the Ge surface a *c*(8×10) appears which is metastable and closely related to the (16×2) [98G,03I]. Although discussed at some length by Hamers [97H1], the early proposed structures for these surfaces turned out to be incorrect. In the ensuing years studies were performed by many authors, with a relatively early result of exceptional clarity being the work of Gai et al. [98G] for the *c*(8×10) surface, revealing characteristics pentagons, as pictured in Fig. 28. The same pentagonal features are seen on the (16×2) surface, associated with five-membered Ge clusters [03I].

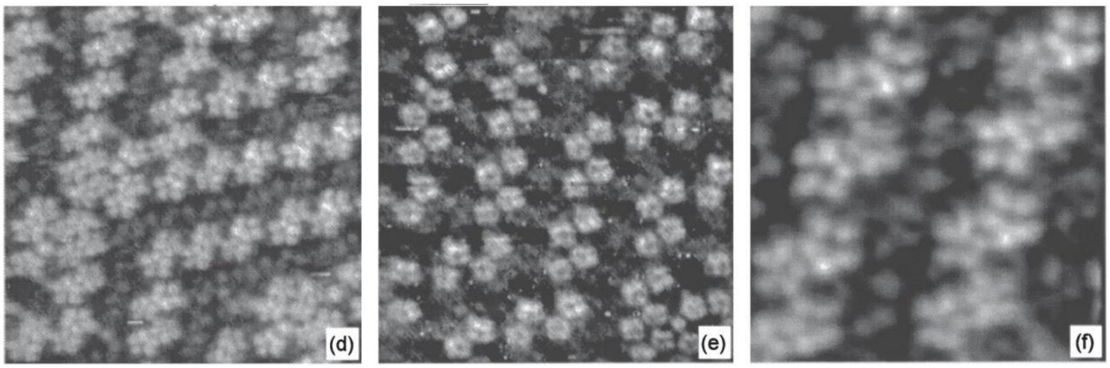

Fig. 28. STM data obtained from Ge(110): (a) empty-state image of *c*(8×10) area (130×130 Å, 1.2 V, 1.5 nA); (b) filled-state image of *c*(8×10) area (130×130 Å, −1.6 V, 0.5 nA); (c) empty-state image image of four *c*(8×10) unit cells (54×54 Å, 1.2 V, 1.5 nA) [98G].

Ge(111)

For the (2×1) reconstructed surfaces of Ge and Si, the basic structure is the same as discussed by Hamers [97H1], the π-ponded chain model. However, the sense of the tilt or "buckling" of the chains has been the topic of recent investigation. For Ge, employing voltage-dependent STM imaging and comparison to theory, this buckling is found experimentally to be in the "negative" direction [04N]. For the *c*(2×8) reconstructed surface, the structure discussed by Hamers has been further verified with more recent voltage-dependent imaging [98L1,09R].

Ge(103)

Ge(103) surfaces studied by STM have been found to contain, in addition of large (1×4) reconstructed areas, tent-like protrusions consisting of (105) {216} and {8,1,16} facets. A (1×1) reconstruction is observed on the (216) surface, and a (1×2) reconstruction on the (105) surface [97G1].

Ge(105)

During epitaxial growth of Ge on Si(100) surfaces, small Ge-rich pyramids or "hut clusters" form [90M]. These pyramids are bounded by Ge/Si(105) facets, with a unique (1×2) reconstruction that intrinsically involves the strain in the system [02F,02R1,04C,10A].

InAs, Indium Arsenide

InAs(100)

The MBE-grown InAs(100) surface is found by STM to have a range of surface reconstructions depending on its stoichiometry [00R2], somewhat similar to the structures found for GaAs(100). When forming InAs/GaSb interfaces, the stoichiometry is also found to affect the interface roughness [99N]. Images of this surface have been obtained at high temperatures, during MBE growth [06T]. Additionally, STM imaging has been performed on samples that have been capped with As, transferred through air, and then decapped in the STM chamber [08S]. Some unique surface structures for In-rich samples prepared by this method have been observed [09F].

InAs(110)

The InAs(110) surface is well known for the fact that strong downwards band bending occurs at the surface, such that the Fermi energy resides several tenths of an eV *above* the conduction band minimum at the surface. The resulting surface accumulation layer has a strong spectroscopic signature in STS, as seen in early low-temperature work on this surface [98C]. The downwards band bending also enables STM imaging at voltages that are normally within the band gap region [03K1].

InAs(111)

Similar to the (110) surface of InAs, its (111) surface also displays downwards band bending and formation of a surface accumulation layer. Niimi et al. studied by STS the formation of Landau levels in this accumulation layer by applying a perpendicular magnetic field [07N], as shown in Fig. 29.

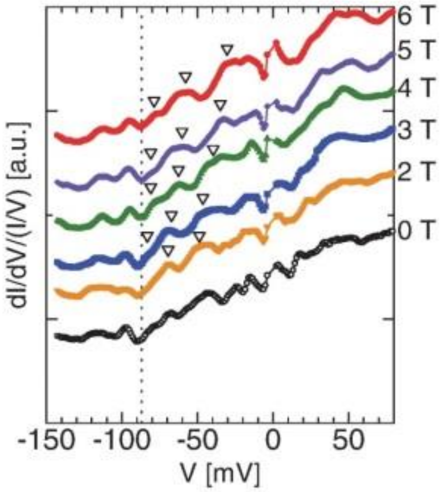

Fig. 29. Normalized STS, *(dI/dV)/(I/V)*, for InAs(111) at the magnetic fields indicated. Each spectrum is vertically shifted for clarity. The locations of Landau levels are indicated by triangular markers. [07N].

InP, Indium Phosphide

InP(100)

InP(001) surfaces grown by metal-organic vapor-phase epitaxy (MOVPE) have been studied by STM, with the surfaces capped in the growth chamber with a P/As sandwich layer and then that layer removed in the STM chamber by thermal desorption [96E2]. An In-rich (2×4) surface structure was found. Using interconnected growth and STM chambers, a P-rich (2×1)/(2×2) surface structure was prepared and imaged [99V,00V]. Its structure is argued to consist of P dimers residing on a complete P layer. Prolonged annealing of the surface produces *p*(2×2) and *c*(4×2) structures, believed to consist of P dimers on a complete In layer underneath.

InN, Indium Nitride

InN($11\bar{2}0$)

The $(11\bar{2}0)$ surface of InN has been prepared by cleavage [11E]. No obvious reconstruction of the surface is found and it is found to be quite sensitive to contamination. The contamination can produce an electron accumulation layer at the surface, which is thus found to be an *extrinsic* surface property.

Si, Silicon

Si(100)

The basic structure of Si(100) is the same as reported by Hamers [97H1]. Additional low-temperature STM results for the surface, relating to buckling of the surface dimers, are reported by Ono et al. [03O].

Si(110)

As discussed above for Ge(110), the (110) surfaces of both Si and Ge form very complex arrangements with nearly (16×2) symmetry. Recent works have demonstrated good progress towards arriving at a convincing structural model for this surface [00A,09S,12N].

Si(111)

As discussed above for Ge(111), recent works have focused on the determination of the sense of the "buckling" for the (2×1) π-bonded chains on the (111) surfaces of Si and Ge. Two recent low-temperature studies have determined that the Si(111)-(2×1) surface contains *both* positively and negatively buckled areas [11B,12L], as illustrated in Fig. 30. The negatively buckled areas occur only on heavily *n*-type material, for which electron transfer from positively to negatively buckled areas provides a driving force for the formation of the latter.

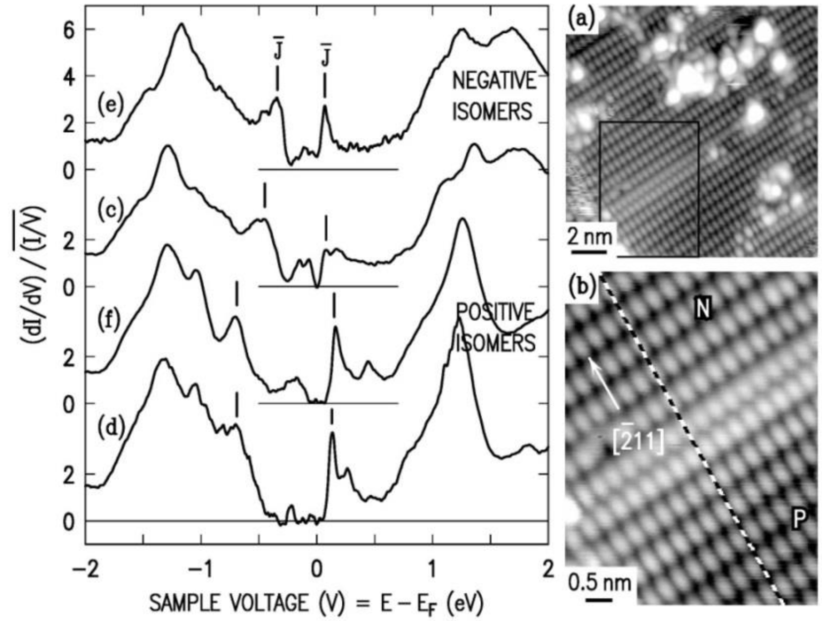

Fig. 30. **(a)** and **(b)** STM images from cleaved Si(111), acquired at 8 K and with sample-tip voltage of -1.0 V. Image **(b)** shows an expanded view of the area indicated in **(a)**. Gray scale ranges are **(a)** 0.22 and **(b)** 0.12 nm. Tunneling spectra acquired from near the N and P symbols in image **(b)** are shown by curves **(c)** and **(d)**, respectively. Spectra acquired from neighboring surface regions are shown by **(e)** and **(f)** [11B].

Si(113)

The (113) surface of Si is somewhat unique in that it is a high-index surface, but one with a relatively low surface energy, i.e., comparable to that of the low-index Si surfaces [91K]. The (3×2) reconstruction on this surface is complex, but nevertheless understandable in terms of several basic units: a pentamer (five-membered cluster) above an interstitial atom, an adatom, and a tetramer (four-membered cluster) [94D,96W]. Figure 31 shows a comparison of theory and STM experiment for this surface.

a) Measured STM images:

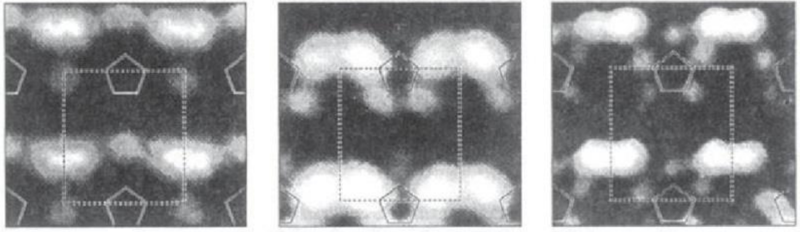

b) Computer simulations for the subsurface interstitialcy model:

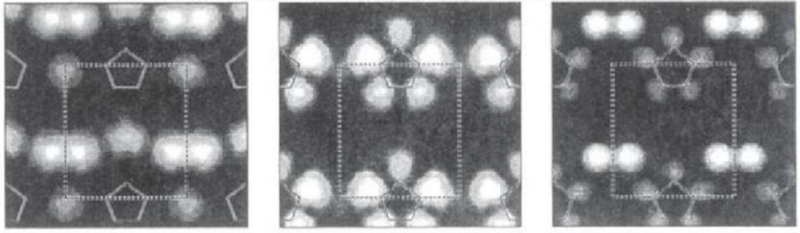

Fig. 31. STM images of the Si(113) surface and their calculated counterparts. The broken lines mark surface elementary cells. The left column shows occupied states (measured at -2.0 V, 2.0 nA), the middle and the right column show empty states (measured at 1.5 V, 1.0 nA and 3 V, 2 nA, correspondingly). **(a)** Experimental STM images. Note the pentagonal structure, clearly visible around the sketched pentagon in the images of empty states. **(b)** LDOS for the 3×2 interstitialcy model. The pentagonal structure of the surface is properly reproduced [94D].

Si(112), (114), (335), (337), (5,5,12)

A variety of high-index Si surfaces have been studied by Baski and co-workers [97B]. The (112) surface is found to reconstruct into nm-scale (111) and (337) facets, and similarly for the (335) surface [95B2]. The (114) surface forms a (2×1) reconstruction that is a natural extension of vicinal (100) surfaces, with the structure including dimers, tetramers, and rebonded step edge atoms [96E1]. The (5,5,12) surface forms a very large (2×1) unit cell which can be viewed as a combination of two (337) unit cells (with distinctly different structures) and a single (225) unit cell [95B1].

SiC, Silicon Carbide

SiC(100)

SiC in its cubic form is less common than its hexagonal form, but nevertheless some STM studies have been performed on the (100) surface. A semiconducting *c*(4×2) structure identified as rows of Si dimers that are alternated raised and lowered along a row [97S3]. At elevated temperatures above 400 °C this surface is found to transform to a metallic (2×1) structure with all dimers at the same height [97Y2]. A different (3×2) arrangement of dimers has also been imaged on this surface [96S].

SiC(0001) and $(000\bar{1})$

A family of surface reconstructions exists on the SiC(0001) and $(000\bar{1})$ surfaces, depending on the surface stoichiometry. For (0001), going from Si-rich to C-rich, unit cells of (3×3), (√3×√3)*R*30°, (5×5), and (6√3×6√3)*R*30° have been studied by STM [96L,96O,97M,97S4]. The (3×3) surface consists of a twisted Si-rich adlayer with clover-like rings [98S3]. The (√3×√3)*R*30° surface consists for a bulk terminated surface covered with Si adatoms [95O]. Whereas a metallic surface is expected for that structure, STS and other measurements indicate an insulating surface [99R], which is interpreted in terms of a Mott-Hubbard insulator [98N1]. A similar interpretation is made for the case of the (3×3) surface [00G1]. A (2√3×2√3)*R*30° surface phase is found to be intermediate between the (3×3) and the (√3×√3)*R*30° [04A], and it appears most commonly on cubic SiC(111) formed on Si(111) [98P,01Y]. The (5×5) surface contains small clusters, or multimers, containing 2 – 7 subunits [96O]. The detailed structure of these subunits is not presently known, although STS of the structure is reported to be similar to that of the (6√3×6√3)*R*30° surface, suggesting a common origin [09N]. The (6√3×6√3)*R*30° surface often appears as nearly (6×6) in STM, and the same structure is also seen on cubic SiC(111) surfaces. [91C]. This reconstruction consists of a carbon-rich layer with complex structure containing hexagon-pentagon-heptagon defects [10Q], that acts as a template for subsequent formation of graphene (or graphite) on the surface.

For the $(000\bar{1})$ surface, much less is known about its reconstructions compared to the situation for SiC(0001). Going from Si-rich to C-rich for $(000\bar{1})$, unit cells of $(2\times2)_{Si}$, $(2\times2)_{C}$, and (3×3) have been reported, with the subscripts referring to different Si- or C-rich structures. Initial STM studies have performed [97H2,99B], although definitive structures for these reconstructions are not presently known.

SiC$(11\bar{2}0)$

The $(11\bar{2}0)$ surface of 6H-SiC has been obtained by cleavage [07B1]. No reconstruction is found, although some relaxation of the Si atoms downwards into the bulk is detected by a comparison of experiment and theory. The stacking sequence of the 6H-SiC is clearly apparent in the STM images.

References

90M Mo, Y.-M., Savage, D. E., Swartzentruber, B. S., Lagally, M. G.: Phys. Rev. Lett. **65** (1990) 1020.
91C Chang, C.S., Tsong, I. S. T., Wang, Y. C., Davis, R. F.: Surf. Sci. **256** (1991), 354.
91K Knall, J., Pethica, J. B., Todd, J. D., Wilson, J. H.: Phys. Rev. Lett. **66** (1991) 1773.
94D Dąbrowski, J., Müssig, H.-J., Wolff, G.: Phys. Rev. Lett. **73** (1994) 1660.
95B1 Baski, A. A., Erwin, S. C., Whitman, L., J.: Science **269** (1995) 1556.
95B2 Baski, A. A., Whitman, L. J.: Phys. Rev. Lett. **74** (1995) 956.
95O Mårtensson, P., Owman, F.: Surf. Sci. **330** (1995) L639.
95W Wassermeier, M., Sudijono, J., Johnson, M. D., Leung, K. T., Orr, B. G., Däweritz, L., Ploog, K. H.: Phys. Rev. B **51** (1995) 14721.
96B Behrend, J. Wassermeier, M., Braun, W., Krispin, P., Ploog, K. H.: Phys. Rev. B **53** (1996) 9907.
96E1 Erwin, S. C., Baski, A. A., Whitman, L. J.: Phys. Rev. Lett. **77** (1996) 687.
96E2 Esser, N., Resch-Esser, U., Pristovsek, M., Richter, W.: Phys. Rev. B **53** (1996) 53.
96L Li, L., Tsong, I. S. T.: Surf. Sci. **351** (1996) 141.
96O Owman, F., Mårtensson, P.: Surf. Sci. **369** (1996) 126.
96S Semond, F., Soukiassian, P., Mayne, A., Dujardin, G., Douillard, L., Jaussand, C..: Phys. Rev. Lett. **77** (1996) 2013.
96W Wolff, G., Müssig, H.-J., Dąbrowski, J., Arabczyk, W., Hinrich, S.: Surf. Sci. **357-358** (1996) 667.
97A Avery, A. R., Tok, E. S., Jones, T. S.: Surf. Sci. **376** (1997) L397.
97B Baski, A. A., Erwin, S. C., Whitman, L., J.: Surf. Sci. **392** (1997) 69.
97G1 Gai, Z., Zhao, R. G., Ji, H., Li, X., and Yang, W. S.: Phys. Rev. B **56** (1997) 12308.
97G2 Giesen, M., Linke, U., Ibach, H.: Surf. Sci. **389** (1997) 264.
97H1 Hamers, R., *Scanning Tunneling Microscopy*, in G. Chiarotti (Ed.): The Physics of Solid Surfaces, Landolt–Börnstein, New Series III/24 (Springer, Berlin, Heidelberg 1993–1996).
97H2 Hoster, H. E., Kulakov, M. A., Bullemer, B.: Surf. Sci. **382** (1997) L658.
97K Kuntze, J., Bömermann, J., Rauch, T., Speller, S., Heiland, W.: Surf. Sci. **394** (1997) 150.
97L Li, J. Schneider, W.-D., Berndt, R.: Phys. Rev. B **56** (1997) 7656.
97M Mårtensson, P., Owman, F., Johansson, L. I.: phys. stat. sol. (b) **202** (1997) 501.
97R1 Ritz, G., Schmid, M., Varga, P., Borg, A., M. Rønning: Phys. Rev. B **56** (1997) 10518.
97R2 Rusponi, S., Boragno, C., Valbusa, U.: Phys. Rev. Lett. **78** (1997) 2795.
97S1 Siemens, B., Domke, D., Ebert, Ph., Urban, K.: Phys. Rev. B **56** (1997) 12321.
97S2 Smith, A. R., Feenstra, R. M., Greve, D. W., Neugebauer, J., Northrup, J. E.: Phys. Rev. Lett. **79** (1997) 3934.
97S3 Soukiassian, P., Semond, F., Douillard, L., Mayne, A., Dujardin, G., Pizzagalli, L., Joachim, C.: Phys. Rev. Lett. **78** (1997) 907.
97S4 Starke, U., Schardt, J., Franke, M.: Appl. Phys. A **65** (1997) 587.
97T Thibado,P. M., Bennett, B. R., Shanabrook, B. V., Whitman, L. J.: J. Cryst. Growth. **175/176** (1997) 317.
97X Xue, Q.-K., Hashizume, T., Sakurai, T.: Prog. Surf. Sci. **56** (1997) 1.

97Y1 Yamaguchi, H., Belk, J. G., Zhang, X. M., Sudijono, J. L., Fahy, M. R., Jones, T. S., Joyce, B. A.: Appl. Surf. Sci. **112** (1997) 138.
97Y2 Yu, V., Douillard, L., Fauchoux, O., Soukiassian, P.: Phys. Rev. Lett. **79** (1997) 3700.
98B Bürgi, L., Jeandupeux, O., Hirstein, A., Brune, H., Kern, K.: Phys. Rev. Lett. **81** (1998) 5370.
98C Canali, L., Wildöer, J. W. G., Kerkhof, O., Kouwenhoven, L.P.: Appl. Phys. A **66** (1998) S113.
98G Gai, Z., Zhao, R. G., Yang, W. S.: Phys. Rev. B **57** (1998) R6795.
98K1 Koch, R., Sturmat, M.: Surf. Sci. **402-404** (1998) 861.
98K2 Kuntze, J., Speller, S., Heiland, W.: Surf. Sci. **402-404** (1998) 764.
98L1 Lee, G. Mai, H., Chizhov, I., Willis, R. F.: J. Vac. Sci. Technol. A **16** (1998) 1006.
98L2 Li, L., Han, B.-K., Law, D., Begarney, M., Hicks, R. F.: J. Cryst. Growth **195** (1998) 28.
98L3 Li, J., Schneider, W.-D., Berndt, R.: Appl. Phys. A. **66** (1998) S167.
98L4 Li, J., Schneider, W.-D., Berndt, R., Bryant, O. R., Crampin, S.: Phys. Rev. lett. **81** (1998) 4464.
98L5 Li, J., Schneider, W.-D., Berndt, R. Crampin, S.: Phys. Rev. lett. **80** (1998) 3332.
98M Méndez, J., Gómez-Herrero, J., Pascual, J. I., Baró, A. M.: Appl. Phys. A. **66** (1998) S767.
98N1 Northrup, J. E., Neugebauer, J.: Phys. Rev. B **57**, R4230 (1998).
98N2 Nosho, B. Z., Weinberg, W. H., Zinck, J. J., Shanabrook, B. V., Bennett, B. R., Whitman, L. J.: J. Vac. Sci. Technol. B **16** (1998) 2381.
98P Pascual, J. I., Gómez-Herrero, Baró, A. M.: Surf. Sci. **397** (1998) L267.
98S1 Shaikhutdinov, S. K.: Surf. Sci. **395** (1998) L215.
98S2 Smith, A. R., Feenstra, R. M., Greve, D. W., Shin, M. S., Skowronski, M., Neugebauer, J., Northrup, J. E.: J. Vac. Sci. Technol. B **16** (1998) 2242.
98S3 Starke, U., Schardt, J., Bernhardt, J., Franke, M., Reuter, K., Wedler, H., Heinz, K., Furthmüller, J., Käckell, P., Bechstedt, F.: Phys. Rev. Lett. **80** (1998) 758.
99B Bernhardt, J., Nerding, M., Starke, U., Heinz, K.: Mater. Sci. Eng. **B61-62** (1999) 207.
99G Geelhaar, L., Márquez, J., Jacobi, K., Kley, A., Ruggerone, P., Scheffler, M.: Microelectronics Journal **30** (1999) 393.
99H Held, R., Nowak, G., Ishaug, B. E., Seutter, S. M., Parkhomovsky, A., Dabiran, A. M., Cohen, P. I., Grzegory, I., Porowski, S.: J. Appl. Phys. **85** (1999) 7697.
99J Joyce, B. A., Vvedensky, D. D., Jones, R. S., Itoh, M., Bell, G. R., Belk, J. G.: J. Cryst. Growth **201/202** (1999) 106.
99K Koch, R., Schulz, J. J., Rieder, K.-H.: Europhys. Lett. **48** (1999) 554.
99L Li, J. Schneider, W.-D., Crampin, S., Berndt, R.: Surf. Sci. **422** (1999) 95.
99N Nosho, B. Z., Weinberg, W. H., Barvosa-Carter W., Bennett, B. R., Shanabrook, B. V., Whitman, L. J.:Appl. Phys. Lett. **74** (1999) 1704.
99R Ramachandran, V., Feenstra, R. M.: Phys. Rev. Lett. **82** (1999) 1000.
99S Smith, A. R., Feenstra, R. M., Greve, D. W., Shin, M. S., Skowronski, M., Neugebauer, J., Northrup, J. E.: Surf. Sci. **423** (1999) 70.
99V Vogt, P., Hannappel, Th., Visbeck, S., Knorr, K., Esser, N., Richter, W.: Phys. Rev. B **60** (1999) R5117.
99X Xie, M. H., Seutter, S. M., Zhu, W. K., Zheng, L. X., Wu, H., Tong, S. Y.: Phys. Rev. Lett. **82** (1999) 2749.
00A An, T., Yoshimura, M., Ono, I., Ueda, K.: Phys. Rev. B **61** (2000) 3006.
00B1 Braun, K.-F., Fölsch, S., Meyer, G., Rieder, K.-H.: Phys. Rev. Lett. **85** (2000) 3500-3503.
00B2 Bremer, J., Hansen, J. K., Stahrenberg, K., Worren, T.; Surf. Sci. **429** (2000) 39.
00G1 Gasparov, V. A., Riehl-Chudoba, M., Schröter, B., Richter, Wo.: Europhys. Lett. **5** (2000) 527.
00G2 Gilarowski, G., Méndez, J., Niehus, H.: Surf. Sci. **448** (2000) 290.
00H Hoogeman, M.S., Klik, M. A. J., Schlößer, D. C., Kuipers, L., Frenken, J. W. M.: Surf. Sci. **448** (2000) 142.
00J Jacobi, K., Geelhaar, L., Márquez, J., Platen, J., Setzer, C.: Appl. Surf. Sci. **166** (2000) 173.
00K Koch, R., Sturmat, M., Schulz, J. J.: Surf. Sci. **454-456** (2000) 543.
00M1 McAvoy, T., Zhang, J. Waldfried, C., McIlroy, D. N., Dowben, P. A., Zeybek, O., Bertrams, T., Barrett, S.: Eur. Phys. J. B **14** (2000) 747.

00M2 Márquez, J., Geelhaar, L., Jacobi, K.: Phys. Rev. B **62** (2000) 9969.

00N Northrup, J. E., Neugebauer, J., Feenstra, R. M., Smith, A. R.: Phys. Rev. B 61 (2000) 9932.

00R1 Ramachandran, V., Lee, C. D., Feenstra, R. M., Smith, A. R., Northrup, J. E., Greve, D. W.: J. Cryst. Growth **209** (2000) 355.

00R2 Ratsch, C., Barvosa-Carter W., Grosse, F., Owen, J. H. G., Zinck, J. J.: Phys. Rev. B **62** (2000) R7719.

00R3 Repain, V., Berroir, J. M., Rousset, S., Lecoeur, J.: Appl. Surf. Sci. **162-163** (2000) 30.

00S1 Schlößer, D. C., Morgenstern, K., Verheij, L. K., Rosenfeld, G., Besenbacher, F., Comsa, G.: Surf. Sci. **465** (2000) 19.

00S2 Schulz, J. J., Koch, R.: Chem. Phys. Lett. **331** (2000) 119.

00S3 Schulz, J. J., Sturmat, M., Koch, R.: Phys. Rev. B **62** (2000) 15402.

00V Vogt, P., Frisch, A. M., Hannappel, Th., Visbeck, S., Willig, F., Jung, Ch., Follath, R., Braun, W., Richter, W.: Appl. Surf. Sci. **166** (2000) 190.

00X Xue, Q. K., Xue, Q. Z., Kuwano, S., Sakurai, T., Ohno, T., Tsong, I. S. T., Qiu, X. G., Segawa, Y.: Thin Solid Films **367** (2000) 149.

01B1 Bischoff, M. M. J., Konvicka, C., Quinn, A. J., Schmid, M., Redinger, J., Podloucky, R., Varga, P., van Kempen, H.: Phys. Rev. let. **86** (2001) 2396.

01B2 Bobrov, K., Mayne, A. J., Dujardin, G.: Nature **413** (2001) 616.

01C Costantini, G., Rusponi, S., de Mongeot, F. B., Boragno, C., Valbusa, U.: J. Phys: Condens. Matter **13** (2001) 5875.

01D Dulot, F., Turban, P., Kierren, B., Eugéne, J., Alnot, M., Andrieu, S.: Surf. Sci. **473** (2001) 172.

01F Farrell, H. H., Lu, L., Schultz, B. D., Denison, A. B., Palmstrøm, C. J.: J. Vac. Sci. Technol. B **19** (2001) 1597.

01H Hofer, W. A., Redinger, J., Biedermann, A., Varga, P.: Surf. Sci. **482-485** (2001) 1113.

01K Koch, R., Schulz, J. J.: Phys. Rev. Lett. **87** (2001) 039604.

01M1 Márquez, J., Geelhaar, L., Jacobi, K.: Appl. Phys. Lett. **78** (2001) 2309. *erratum* Eisele, H., Jacobi, K.: Appl. Phys. Lett. **90** (2007) 129902.

01M2 Morgenstern, K., Rosenfeld, G., Cosma, G., Sørensen, M. R., Hammer, B., Lægsgaard, E., Besenbacher, F.: Phys. Rev. B. **63** (2001) 045412.

01M3 Mugarza, A., Mascaraque, A., Pérez-Dieste, V., Repain, V., Rousset, S., García de Abajo, F. J., Ortega, J. E.: Phys. Rev. Lett. **87** (2001) 107601.

01O Ohtake, A., Nakamura, J., Komure, T., Hanada, T., Yao, T., Kuramochi, H., Ozeki, M.: Phys. Rev. B **64** (2001) 045318.

01R Rost, M. J., Frenken, J. W. M.: Phys. Rev. Lett. **87** (2001) 039603.

01T Töben, L., Hannappel, T., Möller, K., Crawack, H.-J., Pettenkofer, C., and Willig, F.: Surf. Sci. **494** (2001) L755.

01Y Yang, J., Wang, X.-s., Guang-jie, Z., Cue, N., Wang, X.: Surf. Sci. **476** (2001) 1.

02B Bischoff, M. M. J., Konvicka, C., Quinn, A. J., Schmid, M., Redinger, J., Podloucky, R., Varga, P., van Kempen, H.: Surf. Sci. **513** (2002) 9.

02C Christiansen, J., Morgenstern, K., Schiøtz, J., Jacobsen, K. W., Braun, K.-F., Rieder, K.-H., Lægsgaard, E., Besenbacher, F.: Phys. Rev. Lett. **88** (2002) 206106.

02F Fujikawa, Y., Akiyama, K., Nagao, T., Sakurai, T., Lagally, M. G., Hashimoto, T., Morikawa, Y., Terakura, K.: Phys. Rev. Lett. **88** (2002) 176101.

02M1 Márquez, J., Geelhaar, L., Jacobi, K.: Phys. Rev. B **65** (2002) 165320.

02M2 Morgenstern, K., Braun, K.-F., Rieder, K.-H.: Phys. Rev. Lett. **89** (2002) 226801.

02N Ney, A., Schulz, J. J., Sturmat, M., Koch, R.: Surf. Sci. **519** (2002) 192.

02R1 Raiteri, P., Migas, D. B., Miglio, L., Rastelli, A., von Känel, H.: Phys. Rev. Lett. **88** (2002) 256103.

02R2 Reinecke, N., Reiter, S., Vetter, S., Taglauer, E.: Appl. Phys. A. **75** (2002) 1.

02S1 Schmidt, A., Meier, W., Hammer, L., Heinz, K.: J. Phys.: Condens. Matter **14** (2002) 12353.

02S2 Suzuki, T., Temko, Y., Jacobi, K.: Surf. Sci. **511** (2002) 13.

02Y Yagi-Watanabe, K., Suzuki, D., Fukutani, H.: Surf. Sci. **518** (2002) 155.

03B1 Bertals, L., Hla, S.-W., Kühnle, A., Meyer, G., Rieder, K.-H., Manson, J. R.: Phys. Rev. B **67** (2003) 205416.

03B2 Bobrov, K., Mayne, A., Comtet, G., Dujardin, G., Hellner, L., Hoffman, A.: Phys. Rev. B **68** (2003) 195416.

03I Ichikawa, T.: Surf. Sci. **544** (2003) 58.

03K1 Klijn, J., Sacharow, L., Meyer, C., Blügel, S., Morgenstern, M., Wiesendanger, R.: Phys. Rev. B **68** (2003) 205327.

03K2 Kralj, M., Pervan, P., Milun, M., Wandelt, K., Mandrino, D., Jenko, M.: Surf. Sci. **526**(2003) 166.

03L1 Lee, C. D., Dong, Y., Feenstra, R. M., Northrup, J. E., Neugebauer, J.: Phys. Rev. B **68** (2003) 205317.

03L2 Lee, C. D., Feenstra, R. M., Northrup, J. E., Lymperakis, L., Neugebauer, J.: Appl. Phys. Lett. **82** (2003) 1793.

03O Ono, M., Kamoshida, A., Matsuura, N., Ishikawa, E., Eguchi, T., Hasegawa, Y.: Phys. Rev. B **67** (2003) 201306(R).

03R Rost, M. J., van Albada, S. B., Frenken, J. W. M.: Surf. Sci. **547** (2003) 71.

03T Tsukamoto, S., Pristovsek, M., Ohtake, A., Orr, B. G., Bell, G. R., Ohno, T., Koguchi, N.: J. Cryst. Growth **251** (2003) 46.

03V Vitali, L., Wahl, P., Schneider, M. A., Kern, K., Silkin, V. M., Chulkov, E. V., Echenique, P. M.: Surf. Sci. **523** (2003) L47.

03W Wahl, P., Schneider, M. A., Diekhöner, L., Vogelgesang, R., Kern, K.: Phys. Rev. Lett. **91** (2003) 106802.

03Z1 Zandvliet, H. J. W.: Phys. Rep. **388** (2003) 1.

03Z2 Zubera, S. M., Szczudlo, Z., Szczepkowicza, A., Losovyi, Ya. B., Ciszewski,A.: Surf. Sci. **95** (2003) 165.

04A Amy, F., Soukiassian, P., Brylinski, C.: Appl. Phys. Lett. **85** (2004) 926.

04C Ciobanu, C. V., Predescu, C.: Phys. Rev. B **70** (2004) 085321.

04M Mirechi Millunchick, J., Riposan, A., Dall B. J., Pearson, C., Orr, B. G.: Surf. Sci. **550** (2004) 1.

04N Nie, S., Feenstra, R. M., Lee, J. Y., Kang, M.-H.: J. Vac. Sci. Technol. A **22** (2004) 1671.

05M Morgenstern, K., Lægsgaard, E., Besenbacher, F.: Phys. Rev. B. **71** (2005) 155426.

05T Temko, Y., Suzuki, T., Zy, M. C., Pötschke, K. Bimberg, D., Jacobi, K.: Phys. Rev. B **71** (2005) 045366.

06B Becker, M., Crampin, S., Berndt, R.: Phys. Rev. B. **73** (2006) 081402.

06C Costina, I., Schmid, M., Schiechl, H., Gajdosˇ, M., Stierle, A., Kumaragurubaran, S., Hafner, J., Dosch, H., Varga, P.: Surf. Sci. **600** (2006) 617.

06E Engbæk, J., Schiøtz, J., Dahl-Madsen, B., Horch, S.: Phys. Rev. B. **74** (2006) 195434.

06K Kuchowicz, M., Stepanovsky, S., Kołaczkiewicz, J.: Surf. Sci. **600** (2006) 1600.

06M Mann, O., Aravinda, C. L., Freyland, W., J. Phys. Chem B **110** (2006) 21521.

06T Tsukamoto, S., Bell, G. R., Arakawa, Y.: Microelectronics Journal **37** (2006) 1498.

06Y Yakovkin, I. N., Kuchowicz, M., Szukiewicz, R., Kołaczkiewicz, J.: Surf. Sci. **600** (2006) L240.

07B1 Bertelli, M., Monoth, J., Wenderoth, M., Rizzi, A., Ulbrich, R. G., Righi, M. C., Bertoni, C. M.: Phys. Rev. B **75** (2007) 165312.

07B2 Bode, M., Krause, S., Berbil-Bautista, L., Heinze, S., Wiesendanger, R.: Surf. Sci. **601** (2007) 3308.

07D Dougherty, D. B., Maksymovych, P., Lee, J., Feng, M., Petek, H., Yates, J. T.: Phys. Rev. B **76** (2007) 125428.

07N Niimi, Y., Kanisawa, K., Kojima, H., Kambara, H., Hirayama, Y., Tarucha, S., Fukuyama, H.: J. Phys.: Conf. Ser. **61** (2007) 874.

08A Albers, B. J., Liebmann, M., Schwendemann, T. C., Baykara, M. Z., Heyde, M., Salmeron, M., Altman, E. I., Schwarz, U. D.: Rev. Sci. Instrum. **79** (2008) 033704.

08B Braun, K.-F., Rieder, K.-H.: Phys. Rev. B **77** 2(2008) 245429.

08I Ivanova, L., Borisova, S., Eisele, H., Dähne, M. , Laubsch, A. , Ebert, Ph.: Appl. Phys. Lett. **93**, 192110 (2008).

08L Liu, Y., Cai, Y., Zhang, L., Xie, M. H., Wang, N., Zhang, S. B., Wu, H. S.: Appl. Phys. Lett. **92** (2008) 231907.

08R Rinehimer, J. A., Widom, M., Northrup, J. E., Feenstra, R. M.: Phys. Stat. Sol. (b) **245** (2008) 920.

08S Shen, J., Winn, D., Melitz, W., Clemens, J., Kummel, A. C.: ECS Transactions **16** (2008) 463.

09B1 Nishimura, Y., Kakeya, M., Higashiguchi, M., Kimura, A., Taniguchi, M., Narita, H., Cui, Y., Nakatake, M., Shimada, K., Namatame, H.: Phys. Rev. B **79** (2009) 245402.

09B2 Bertelli, M., Löptien, P., Wenderoth, M., Rizzi, A., Ulbrich, R. G., Righi, M. C., Ferretti, A., Martin-Samos, L., Bertoni, C. M., A. Catellani, A.: Phys. Rev. B **80** (2009) 115324.

09E Ebert, Ph., Ivanova, L., Borisova, S., Eisele, H., Laubsch, A., Dähne, M.: Appl. Phys. Lett. **94**, (2009) 062104.

09F Feldwinn, D. K., Clemens, J. B., Shen, J., Bishop, S. R., Grassman, T. J., Kummel, A. C., Droopad, R., Passlack, M.: Surf. Sci. **603** (2009) 3321.

09H Heinz, K., Hammer, L.: Prog. Surf. Sci. **84** (2009) 2.

09N Nie, S., Feenstra, R. M.: J. Vac. Sci. Technol. A **27** (2009) 1052.

09R Razado-Colambo, I., He, J., Zhang, H. M., Hansson, G. V., Uhrberg, R. I. G.: Phys. Rev. B **79** (2009) 205410.

09S Sakamoto, K., Setvin, M., Mawatari, K., Eriksson, P. E. J., Miki, K., Uhrberg, R. I. G.: Phys. Rev. B **79** (2009) 045304.

10A Arapkina, L. V., Yuryev, V. A.: Phys. Rev. B **82** (2010) 045315.

10B Braun, K.-F., S.-W. Hla.: Appl. Phys. A. **98** (2010) 583.

10Q Qi, Y., Rhim, H., Sun, G. F., Weinert, M., Li, L.: Phys. Rev. Lett. **105** (2010) 085502.

11B Bussetti, G., Bonanni, B., Cirilli, S., Violante, A., Russo, M., Goletti, C., Chiaradia, P., Pulci, O., Palummo, M., Del Sole, R., Gargiani, P. Betti, M. G., Mariani, C., Feenstra, R. M., Meyer, G., Rieder, K. H.: Phys. Rev. Lett. **106** (2001) 067601.

11E Ebert, Ph., Schaafhausen, S., Lenz, A., Sabitova, A., Ivanova, L., Dähne, M., Hong, Y.-L., Gwo, S., Eisele, H.: Appl. Phys. Lett. **98** (2011) 062103.

12B Bengió, S., Navarro, V., González-Barrio, M. A., Cortés, R., Vobornik, I., Michel, E. G., Mascaraque, A.: Phys. Rev. B. **86** (2012) 045426.

12L Löser, K., Wenderoth, M., Spaeth, T. K. A., Garleff, J. K., Ulbrich, R. G., Pötter, M., Rohlfing, M.: Phys. Rev. B **86** (2012) 085303.

12N Nagasawa, T., Sueoka, K.: J. Electrochem. Soc. **159** (2012) H201.